Research Article

Abdeliazim Mustafa Mohamed*, Bassam A. Tayeh, Yazid Chetbani, Aissa Laouissi, Maaz Osman Bashir, and Yazan Issa Abu Aisheh

Innovative optimization of seashell ash-based lightweight foamed concrete: Enhancing physicomechanical properties through ANN-GA hybrid approach

https://doi.org/10.1515/rams-2025-0131
received March 05, 2025; accepted July 02, 2025

Abstract: This study presents a novel approach to sustainable construction by utilizing three types of seashell ashes, namely, oyster shell ash (OSA), scallop shell ash (SSA), and mussel shell ash (MSA), as partial replacements for cement in lightweight foamed concrete (LFC). This novel application of aquaculture waste as an additive enhances the creation of more sustainable and resilient construction materials for urban settings. The physicomechanical properties of LFC, such as compressive strength (CS), flexural strength (FS), split tensile strength (STS), water absorption (WA), and porosity (*P*), were assessed utilizing response surface methodology (RSM) and artificial neural network (ANN) with *K*-fold cross-validation. The research examines the influence of additive type (OSA, SSA, MSA), curing duration (7–28 days), and additive concentration (0–30%) on the characteristics of LFC. Analysis of variance indicated that curing time exerted the most substantial effect on CS, FS, and STS, but additive content had a more pronounced impact on WA and *P*. The findings indicated favorable enhancements in CS, FS, and STS with curing durations of 28 days and additive concentrations between 4 and 20%. Replacing cement with OSA, SSA, and MSA showed favorable benefits on LFC characteristics. The predictive effectiveness of the DNN-IGWO, ANN, RSM, and Support vector machine models was evaluated using several error metrics, including mean absolute deviation, mean absolute percentage error, root mean square error, and coefficient of determination (R^2). The results showed that the hybrid DNN-IGWO model outperformed all other approaches, providing significantly higher accuracy across all attributes studied. Moreover, the incorporation of evolutionary algorithms utilizing DNN-IGWO models facilitated the discovery of optimal solutions for the multi-objective optimization of LFC properties. The optimization exposed intrinsic trade-offs between targets, such as CS *vs* WA and CS *vs P*, underscoring the necessity for meticulous equilibrium in the optimization process. This study constitutes a notable advancement in sustainable development goals in construction materials by improving concrete characteristics through the incorporation of seashell ash and sophisticated optimization methods.

Keywords: sustainable building, sustainable development goals, lightweight foamed concrete, seashell ash, ANOVA, artificial neural networks, genetic algorithms, response surface methodology, support vector machines, DNN-IGWO, multi-objective optimization

*** Corresponding author: Abdeliazim Mustafa Mohamed**, Department of Civil Engineering, College of Engineering in Al-Kharj, Prince Sattam bin Abdulaziz University, Al-Kharj, 11942, Saudi Arabia, e-mail: a.bilal@psau.edu.sa
Bassam A. Tayeh: Civil Engineering Department, Faculty of Engineering, Islamic University of Gaza, Gaza Strip, P.O. Box 108, Palestine; Dept of Civil & Environmental Engineering, University of Waterloo, Waterloo, ON, Canada, e-mail: btayeh@iugaza.edu.ps
Yazid Chetbani: Centre de Recherche scientifique et Technique en Analyses Physico-Chimiques CRAPC, Technical platform for physico-chemical analysis, University center No. 02, University of Laghouat 03000, Laghouat, Algeria, e-mail: chetbani.yazid92@gmail.com
Aissa Laouissi: Department of Mechanical Engineering, Faculty of Sciences and Technology, University of Bordj Bou Arreridj, Bordj Bou Arreridj 34033, Bordj Bou Arreridj, Algeria, e-mail: aissou_011@yahoo.fr
Maaz Osman Bashir: Department of Civil Engineering, Faculty of Engineering Sciences, Omdurman Islamic University, Khartoum, Sudan
Yazan Issa Abu Aisheh: Hourani Center for Applied Scientific Research (HCASR), Al-Ahliyya Amman, University, Amman 19328, Jordan, e-mail: yabueisheh@hotmail.com

1 Introduction

Lightweight foamed concrete (LFC) is a cellular concrete characterized by its lightweight nature, typically ranging

in density from 400 to 1,850 kg·m^{-3} [1,2]. This material is classified as lightweight concrete, characterized by the presence of random air voids that are evenly distributed throughout the mixture due to the addition of foam agents in the mortar. LFC exhibits high flowability due to the presence of air voids, characterized by low cement content and minimal aggregate usage [3–5]. This concrete, which is classified into air-entrained and foam concrete based on pore formation methods, employs distinct approaches to introduce porosity (*P*) into the material [6,7]. Air-entrained concrete utilizes gas-forming chemicals mixed into mortar, where a chemical reaction during mixing generates gas bubbles, yielding a porous structure; commonly employed aerating agents include aluminum powder, calcium carbide, and hydrogen peroxide [6,8,9].

Foam concrete utilizes mechanical means to form pores, either through a pre-foaming process where a foaming agent is mixed with the water prior to incorporation into the mortar or *via* a mixed foaming process where the foaming agent is directly mixed with the mortar. These methods collectively contribute to the lightweight and insulating characteristics of aerated concrete [10–12].

The investigation of waste use, specifically waste binder particles as replacements for cement in concrete, offers an alternative approach underpinned by multiple reasons. Employing aquaculture waste as substitutes for cement presents considerable potential for improving the characteristics of cementitious materials and promoting ecologically sustainable concrete manufacturing [13,14]. Emerging aquaculture byproducts such as seashells, including oyster shell ash (OSA), scallop shell ash (SSA), and mussel shell ash (MSA), are promising as valuable components in the construction industry, promoting the adoption of more sustainable building practices. In this study, the term “additive type” refers to the different seashell ashes used as partial replacements for cement, namely, OSA, SSA, and MSA. The “additive content” refers to the percentage of cement replaced by these ashes, ranging from 0 to 30% [15–18].

Previous research extensively explored substituting cement with seashell powder in concrete mixes, revealing lengthened setting times, decreased compressive strength (CS) and weakened flexural strength (FS) as notable outcomes. Comparative analyses among seashell varieties, including periwinkle shell ash (PSA), OSA, and snail shell ash (SSA), exhibit differences in water consistency in cement pastes [11,16,19].

Olutoge *et al.* [20] investigated the effects of incorporating PSA into concrete. They found that as the proportion of PSA increased, the compaction factor improved while the slump decreased. Furthermore, higher PSA percentages resulted in longer initial and final setting times. In addition, the specific gravity of PSA was lower than that of ordinary Portland cement (OPC). Finally, the CS of concrete specimens decreased with increasing proportions of PSA.

Hai-Yan *et al.* [21] delved into the utilization of crushed oyster shell (COS) in marine concrete production, alongside fly ash (FA) and blast furnace slag (BS). Their investigation centered on evaluating the impact of different COS proportions, in conjunction with FA and BS, on the strength and durability of marine concrete. The findings elucidated that incorporating an optimal quantity of COS yielded favorable outcomes on these properties, thereby augmenting the efficacy and sustainability of concrete.

Adeala and Olaoye [22] explored the utilization of SSA as a partial substitute for cement in concrete. Their investigation revealed that when used at a 20% replacement level, SSA-blended concrete exhibited favorable characteristics, including low water absorption (WA) and high CS. These findings imply that SSA concrete may be suitable for structural applications, provided that the replacement level does not surpass 20%.

Several techniques, including response surface methodology (RSM) and artificial neural network (ANN), are utilized to investigate and optimize the properties of cement-based materials [23–25]. RSM, developed by Box and Wilson in 1951, optimizes processes by adjusting factors such as cement composition and curing time in concrete engineering. It aims to enhance outcomes such as CS and durability while minimizing resource usage. This systematic approach reduces the number of experiments required and identifies significant process parameters through analysis of variance (ANOVA). Regression equations predict responses based on given parameters, with response surface plots illustrating their effects [25–27]. Ultimately, the desirability approach is used to optimize process parameters, confirmed through validation tests [28,29].

An ANN is a data processing system structured with layers, including an input layer, one or more hidden layers, and an output layer. Each layer consists of numerous interconnected processing units known as neurons [30–32]. The input layer receives data, which are then processed through the hidden layers. Within these layers, neurons perform computations on the input data, passing it through activation functions to introduce nonlinearity and generate meaningful representations [24,33–35]. The output layer then produces the final result based on the processed information. This interconnected structure allows ANNs to learn complex patterns and relationships within data, making them effective tools for tasks such as classification, regression, and face recognition [30,35].

Rizalman and Lee [36] compared the performance of ANN and RSM in predicting the CS of palm oil fuel ash concrete and found that RSM outperformed ANN with a

Table 1: Experimental results of CS, FS, STS, WA, and *P* of the studied LFC [16]

Sample number	Additive	Additive type	Curing time (days)	Additive content (%)	CS (MPa)	FS (MPa)	STS (MPa)	WA (%)	*P* (%)
1	OSA	1	7	0	9.2	2.1	1.38	15.54	35.10
2		1	14	0	12.2	2.8	1.8	15.22	34.40
3		1	28	0	14.5	3.4	2.3	14.50	33.70
4		1	7	5	9.3	2	1.39	16.80	36.50
5		1	14	5	12.5	2.9	1.9	16.91	35.60
6		1	28	5	14.7	3.5	2.5	15.60	34.90
7		1	7	10	9.5	2.1	1.41	17.57	37.50
8		1	14	10	12.7	2.9	2.1	17.76	36.70
9		1	28	10	15.0	3.6	2.5	16.30	35.90
10		1	7	15	9.8	2.2	1.46	18.08	38.30
11		1	14	15	13.1	3	2.1	18.25	37.50
12		1	28	15	15.4	3.7	2.6	16.75	36.70
13		1	7	20	9.0	2	1.33	18.46	38.9
14		1	14	20	12.2	2.8	1.9	18.65	38.2
15		1	28	20	14.2	3.5	2.5	17.10	37.4
16		1	7	25	8.3	1.8	1.21	18.74	39.3
17		1	14	25	11	2.5	1.7	18.95	38.8
18		1	28	25	13.0	3.1	2.2	17.4	38.1
19		1	7	30	7.3	1.6	1.1	18.97	39.7
20		1	14	30	9.9	2.3	1.6	19.25	39.2
21		1	28	30	11.7	2.8	2	17.70	38.6
22	SSA	2	7	0	9.2	2.1	1.38	15.54	35.1
23		2	14	0	12.2	2.8	1.8	15.22	34.4
24		2	28	0	14.5	3.4	2.3	14.5	33.7
25		2	7	5	9.10	2	1.37	17.06	36.7
26		2	14	5	12.3	2.8	2	17.23	36.1
27		2	28	5	14.5	3.4	2.4	15.9	35.2
28		2	7	10	9.10	2	1.38	17.88	38.0
29		2	14	10	12.4	2.8	1.9	18.03	37.3
30		2	28	10	14.6	3.5	2.4	16.7	36.4
31		2	7	15	9.4	2.1	1.39	18.36	38.9
32		2	14	15	12.7	2.9	2	18.53	38.2
33		2	28	15	14.9	3.6	2.5	17.2	37.4
34		2	7	20	8.8	1.9	1.30	18.76	39.5
35		2	14	20	11.9	2.7	1.9	18.93	38.8
36		2	28	20	14.1	3.4	2.4	17.6	38.0
37		2	7	25	7.9	1.7	1.18	19.05	40.0
38		2	14	25	10.6	2.5	1.7	19.23	39.3
39		2	28	25	12.6	3	2.1	17.9	38.6
40		2	7	30	6.9	1.5	1.04	19.27	40.4
41		2	14	30	9.4	2.2	1.4	19.53	39.7
42		2	28	30	11.1	2.7	1.9	18.2	39.0
43	MSA	3	7	0	9.2	2.1	1.38	15.54	35.1
44		3	14	0	12.2	2.8	1.8	15.22	34.4
45		3	28	0	14.5	3.4	2.3	14.5	33.7
46		3	7	5	9.5	2.1	1.42	16.61	36.1
47		3	14	5	12.9	3	2.1	16.63	35.2
48		3	28	5	15.1	3.6	2.6	15.2	34.7
49		3	7	10	10.1	2.2	1.53	17.21	36.9
50		3	14	10	13.6	3.1	2.2	17.43	36.1
51		3	28	10	15.9	3.8	2.7	15.8	35.5
52		3	7	15	10.3	2.3	1.56	17.61	37.6
53		3	14	15	14.0	3.2	2.3	17.83	36.9
54		3	28	15	16.3	4	2.8	16.2	36.2

(*Continued*)

Table 1: *Continued*

Sample number	Additive	Additive type	Curing time (days)	Additive content (%)	CS (MPa)	FS (MPa)	STS (MPa)	WA (%)	*P* (%)
55		3	7	20	9.4	2.1	1.41	17.91	38.2
56		3	14	20	12.7	2.9	2.1	18.13	36.7
57		3	28	20	14.9	3.6	2.5	16.5	36.9
58		3	7	25	8.3	1.8	1.23	18.11	38.7
59		3	14	25	11.2	2.6	1.8	18.33	38.2
60		3	28	25	13.1	3.2	2.2	16.7	37.5
61		3	7	30	7.6	1.7	1.13	18.31	39.1
62		3	14	30	10.3	2.4	1.6	18.53	38.7
63		3	28	30	12.0	3	2.1	16.9	38.0

coefficient of determination (R^2) closer to 1. All the predicted results by RSM fell within a 10% margin of the experimental results, whereas the ANN model had three predicted results outside this margin.

Yaro *et al.* [37] highlighted the superior applicability of the ANN model compared with the RSM model. The ANN model demonstrates greater potential due to its capacity to simulate a broader array of nonlinear polynomials, unlike the RSM model, which is confined to capturing solely quadratic approximations. The ANN model's adeptness in handling nonlinear relationships accounts for its superior performance.

Ray *et al.* [38] found that RSM models are better at predicting concrete properties compared with ANN models. This conclusion is supported by RSM models exhibiting higher determination coefficients (R^2) near 1 and lower error values compared with ANN models. Thus, RSM is the more effective approach for forecasting concrete properties based on the investigated parameters.

This work is a continuation of the research by Maglad *et al.* [16] on seashell ash-based LFC. They conducted an experimental companion to evaluate CS, FS, split tensile strength (STS), WA, and *P* of LFC containing OSA, SSA, and MSA. The results are used in this research to develop models for estimating the five properties of LFC by varying additive types and content and curing duration. For this purpose, RSM, ANN, and genetic algorithm (GA) optimization are applied.

2 Materials

Maglad *et al.* [16] studied the evaluation of physicomechanical properties of seashell ash-based LFC by partially replacing OPC with OSA, SSA, and MSA. The study conformed to BS EN 197-1 standards [39] for OPC and utilized clean river sand as the fine aggregate, with a maximum particle size of 4.75 mm and a specific gravity of 2.53, as per ASTM C33-03

Table 2: Statistical parameters of ANOVA

Statistical parameter	Equation	Definition
The squared sum (SS_f)	$SS_f = \frac{N}{N_{n_f}} \sum_{i=1}^{N_{n_f}} (\bar{y}_i - \bar{y})^2$ (8)	To estimate the square of the deviation from the general mean $\bar{y}$: the average response, $\bar{y}_i$: average of the measured responses for each level *i* of the *F*-factor, *N*: the total number of trials, N_{n_f}: the number of levels of each *f* factor.
The squared mean (MS_i)	$MS_i = \frac{SS_i}{dl_i}$ (9)	Is calculated by dividing the squared sum (SS_i) by the number of degrees of freedom (dl_i)
The *F*-value	$F_i = \frac{MS_i}{MS_e}$ (10)	Used to check the compatibility of the mathematical model on the grounds that the calculated *F*-values must be greater than the tabulated *F* MS_e is the mean squared sum of the errors
Contribution (Cont.%)	$Cont.\% = \frac{SS_f}{SS_T} \times 100$ (11)	It shows the contribution of factors (SS_f) to the total variance (SS_T), indicating the degree of percent effect on response
The coefficient of determination (R^2)	$R^2 = \frac{\sum(y_i - \bar{y})^2}{\sum(\bar{y}_i - \bar{y})^2}$ (12)	The ratio of explained variation to total variation, it is a measure of the goodness of fit

standards [40]. Potable water was used in accordance with BS 3148 standards for concrete mixing [41].

The seashell ashes were collected from local fishermen in Teluk Bahang, Penang, Malaysia, and processed by cleaning, drying, baking at 220°C, and grinding into fine ash. These ashes, primarily composed of calcium oxide (CaO), exhibited pozzolanic properties and were tested as cement replacements at 5, 10, 15, 20, 25, and 30%. The chemical composition of the seashell ashes was verified through X-ray fluorescence analysis, and the specific gravities of the ashes were found to be 2.86 for MSA, 2.64 for OSA, and 2.27 for SSA, indicating their suitability for partial cement replacement.

A protein-based foaming agent, diluted with water in a 1:32 ratio, was employed to create foam with a stable density of 65 ± 10 kg·m^{-3}. The LFC mix was prepared with a sand-to-cement ratio of 1.5:1 and a water-to-cement ratio of 0.48. Nineteen different LFC mixtures were prepared, varying the percentage of seashell ash substitution, and the fresh concrete was poured into molds for curing. The specimens were water-cured for 28 days to ensure complete hydration.

The CS of the LFC specimens was evaluated using cube samples (100 mm × 100 mm) according to BS EN 12390-3 standards [42]. FS tests were performed using prism specimens (100 mm × 100 mm × 500 mm) following BS EN 12390-5 standards [43], while the STS was measured using cylindrical specimens (∅ 100 mm × 200 mm) based on BS EN 12390-6 standards [44]. These tests were conducted at 7, 14, and 28 days to assess the concrete's strength performance under axial, bending, and tensile loads.

WA was evaluated in line with ASTM C1403 standards [45], with the specimens oven-dried at 105°C and immersed in water for 24 h to determine their ability to resist moisture infiltration. The *P* of the LFC specimens was determined using a vacuum saturation technique.

3 Experimental results

The data used in this dataset was produced by RSM, resulting in the formulation of 63 distinct mixes of LFC.

Table 3: ANOVA of LFC properties

Source	SS_f	Df	MS_i	*F*-value	*p*-value	Cont.%	Significant
CS (MPa)	303.5	3	101.17	89.42	<0.0001		
A	1.76	1	1.76	1.56	0.2171	0.47536733	No
B	263.62	1	263.62	233.03	<0.0001	71.2024633	Yes
C	38.11	1	38.11	33.69	<0.0001	10.2933232	Yes
Residual	66.75	59	1.13				
Cor total	370.24	62					
FS (MPa)	21.85	3	7.28	115.84	<0.0001		
A	0.126	1	0.126	2	0.1622	0.492957746	No
B	19.91	1	19.91	316.62	<0.0001	77.89514867	Yes
C	1.82	1	1.82	28.91	<0.0001	7.120500782	Yes
Residual	3.71	59	0.0629				
Cor total	25.56	62					
STS (MPa)	11.52	3	3.84	100.58	<0.0001		
A	0.0754	1	0.0754	1.98	0.1651	0.547567175	No
B	10.75	1	10.75	281.62	<0.0001	78.06826434	Yes
C	0.6925	1	0.6925	18.14	<0.0001	5.029048656	Yes
Residual	2.25	59	0.0382				
Cor total	13.77	62					
WA (%)	92.42	3	30.81	102.19	<0.0001		
A	2.06	1	2.06	6.83	0.0113	1.869328494	Yes
B	20.22	1	20.22	67.09	<0.0001	18.34845735	Yes
C	70.13	1	70.13	232.65	<0.0001	63.63883848	Yes
Residual	17.79	59	0.3015				
Cor total	110.2	62					
***P* (%)**	174.5	3	58.17	214.54	<0.0001		
A	2.68	1	2.68	9.87	0.0026	1.406898	Yes
B	19.85	1	19.85	73.2	<0.0001	10.42049451	Yes
C	151.98	1	151.98	560.56	<0.0001	79.78371568	Yes
Residual	16	59	0.2711				
Cor total	190.49	62					

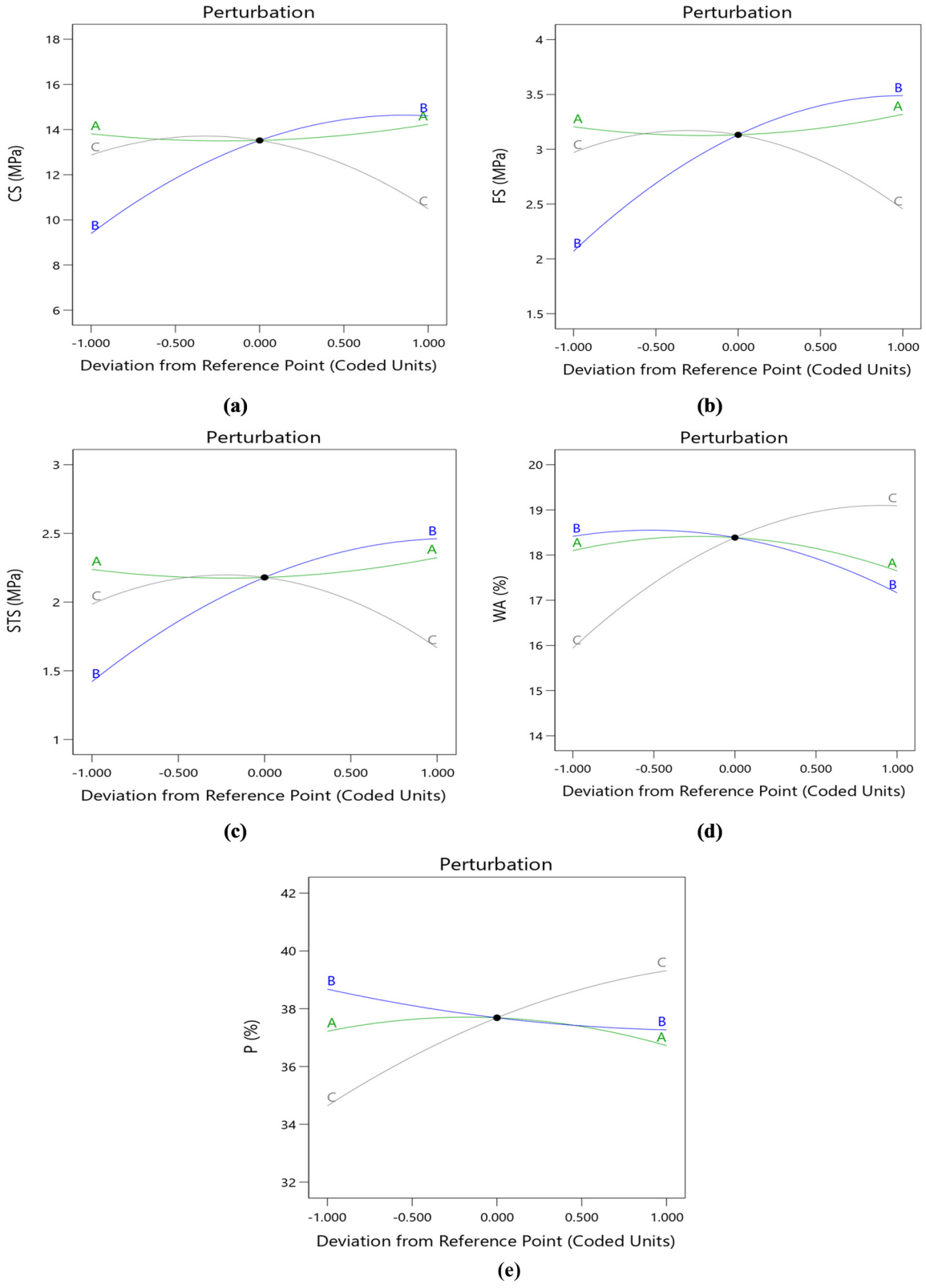

Figure 1: Perturbation plot of (a) CS; (b) FS; (c) STS; (d) WA; and (e) *P*.

The blends were created by modifying several input parameters: the type of seashell ash additive (OSA, SSA, and MSA), curing durations (7, 14, and 28 days), and additive concentrations (0–30%). The three parameters were methodically altered to investigate their collective impact on five principal output properties: CS, FS, STS, WA, and *P*.

Each created blend represents a distinct combination of these elements, enabling us to examine how varying conditions influence the performance of the LFC. The experimental design was organized to guarantee that all pertinent combinations of the variables were included, thereby producing a varied and thorough dataset despite

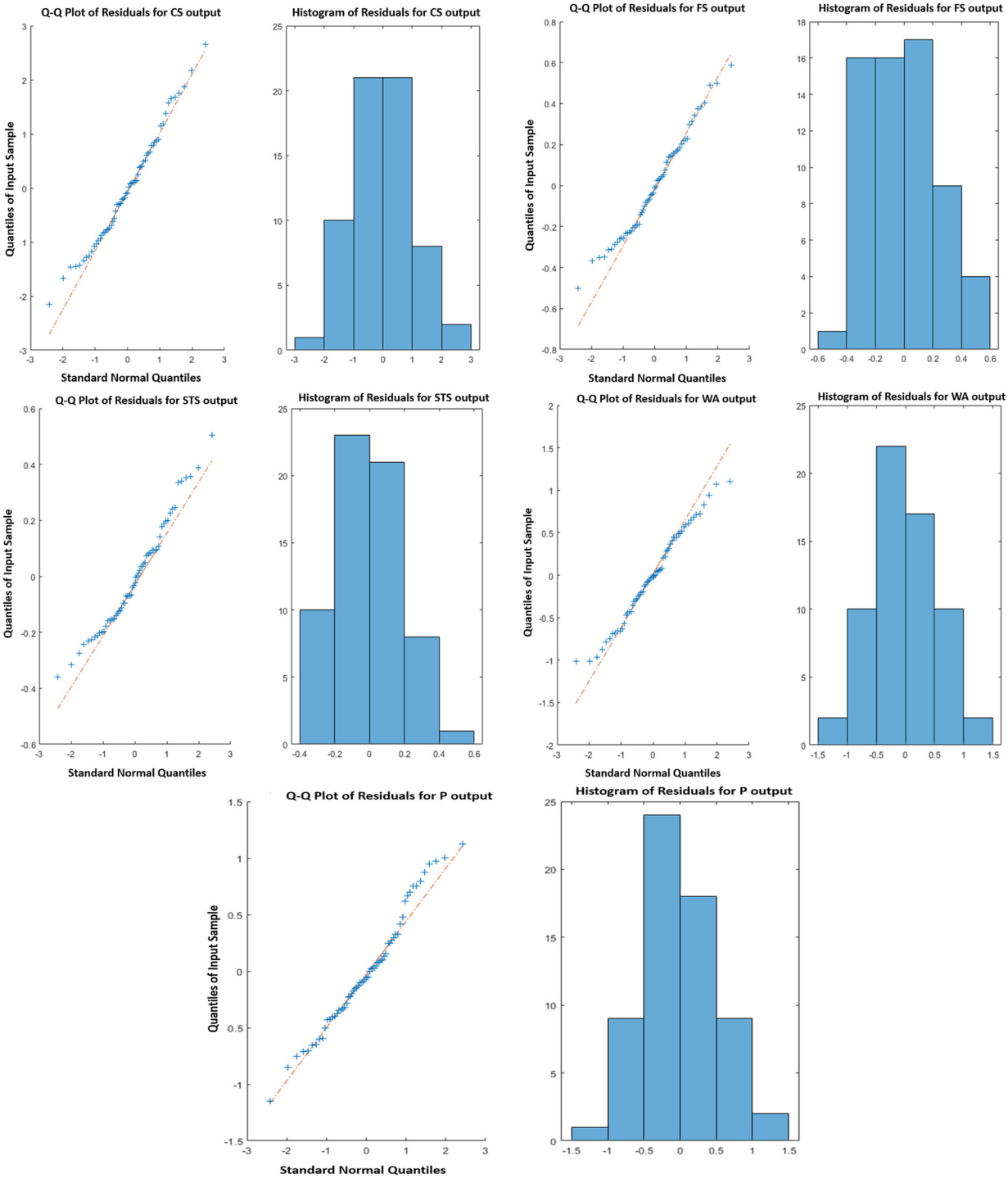

Figure 2: Q–Q plot and histogram of residuals for normality testing after ANOVA analysis.

the limited total amount of data points. The dataset comprises 63 measurements for each of the five properties (CS, FS, STS, WA, and *P*), forming the basis for constructing robust predictive models for these LFC features. All descriptions of the materials and methods are detailed in Maglad *et al.* [16]. The five measured responses of LFC are recorded in Table 1. This database, which counts 63 values of each response, will be used to develop prediction models of the different studied properties.

4 Model development

4.1 RSM modeling

RSM is employed in the first stages of designing experiments to create predictive models for responses and to conduct optimization. These response models may be represented as linear or higher-order polynomials, as seen in the generalized formats specified in Eqs. (1) and (2) [46–49].

$$Y = \beta_0 + \beta_1 X_1 + \beta_2 X_2 + \beta_n X_n + \in, \tag{1}$$

$$Y = \beta_0 + \sum_{i}^{k} \beta_i X_i + \sum_{i}^{k} \beta_{ii} X_i^2 + \sum_{ij}^{k} \beta_{ij} \cdot X_i \cdot X_j + \epsilon, \tag{2}$$

where Y denotes the desired response, β_0 is the regression coefficient for the constant term, and β_i, β_{ii}, and β_{ij} are the coefficients for linear, quadratic, and the interaction of X_i and X_j terms, respectively. The number of factors is denoted by k, while the random error is denoted by $\in$.

RSM offers multiple modeling methodologies, each exhibiting unique attributes and varying degrees of precision. The accuracy of predictive outcomes is influenced not only by the chosen model type but also significantly by the quality and relevance of the experimental data utilized. Accurate model predictions depend on the availability of high-quality, relevant experimental data. This study selected the quadratic model to represent the responses, which include CS, FS, tensile strength, WA, and *P* [50,51]. This model was selected for its superior accuracy compared to other alternatives. The strength of the quadratic model lies in its ability to account for nonlinear effects and complex interactions between input variables, which is vital for achieving reliable predictions when relationships among the variables are not purely linear. These models are expressed in coded terms in Eqs. (3)–(7). Equations expressed in coded factors can be used to predict responses across different levels of each variable. Typically, a value of +1 signifies elevated levels of a factor, whereas a value of −1 denotes low levels by default. The coded equation facilitates the determination of the relative importance of variables by comparing the coefficients of factors, denoted as *A*: (additive type), *B*: (age, fays), and *C*: (additive content, %).

$$\begin{aligned} CS\ (\text{MPa}) = &+ 5.68 - 1.89A + 0.75B + 0.19C \\ &+ 0.0038AB + 0.001AC - 0.002BC \\ &+ 0.50A^2 - 0.014B^2 - 0.01C^2, \end{aligned} \tag{3}$$

$$\begin{aligned} FS\ (\text{MPa}) = &+ 1.26 - 0.51A + 0.18B + 0.04C \\ &+ 0.0016AB + 0.001AC - 0.0002BC \\ &+ 0.13A^2 - 0.003B^2 - 0.002C^2, \end{aligned} \tag{4}$$

$$\begin{aligned} STS\ (\text{MPa}) = &+ 0.76 - 0.37A + 0.13B + 0.039C \\ &+ 0.0005AB - 0.0002AC - 0.0001BC \\ &+ 0.1A^2 - 0.002B^2 - 0.0016C^2, \end{aligned} \tag{5}$$

$$\begin{aligned} WA\ (\%) = &+ 13.2 + 2.03A + 0.14B + 0.25C \\ &- 0.002AB - 0.01AC - 0.0004BC \\ &- 0.51A^2 - 0.005B^2 - 0.004C^2, \end{aligned} \tag{6}$$

$$\begin{aligned} P\ (\%) = &+ 34.19 + 2.69A - 0.17B + 0.26C \\ &+ 0.003AB - 0.009AC + 0.0004BC \\ &- 0.71A^2 + 0.003B^2 - 0.003C^2. \end{aligned} \tag{7}$$

ANOVA is a statistical technique that is widely used in research to analyze and interpret experimental data. It operates on the principles of probability and mathematical statistics, aiming to validate models and evaluate the influence of input parameters on the variability of responses [25,52–55]. ANOVA tests the significance of differences observed among groups or treatments by partitioning the total variance into distinct components attributed to different sources, such as independent variables or interactions [56–59]. This partitioning allows researchers to determine whether the observed differences are statistically significant or merely due to random chance. ANOVA is typically conducted at a 95% confidence interval, denoted by a significance level (α) of 0.05, meaning that results with a *p*-value less than 0.05 are considered statistically significant [60–64]. The statistical parameters taken into account by ANOVA are given in Table 2.

Table 4: Jarque-Bera test *p*-values for residual normality test

Output	*p*-value
CS	0.30916
FS	0.26934
STS	0.13400
W	0.35193
P	0.38533

Note: For all outputs, the *p*-values exceed the significance level (α = 0.05). Therefore, we fail to reject the null hypothesis, and the residuals can be considered normally distributed.

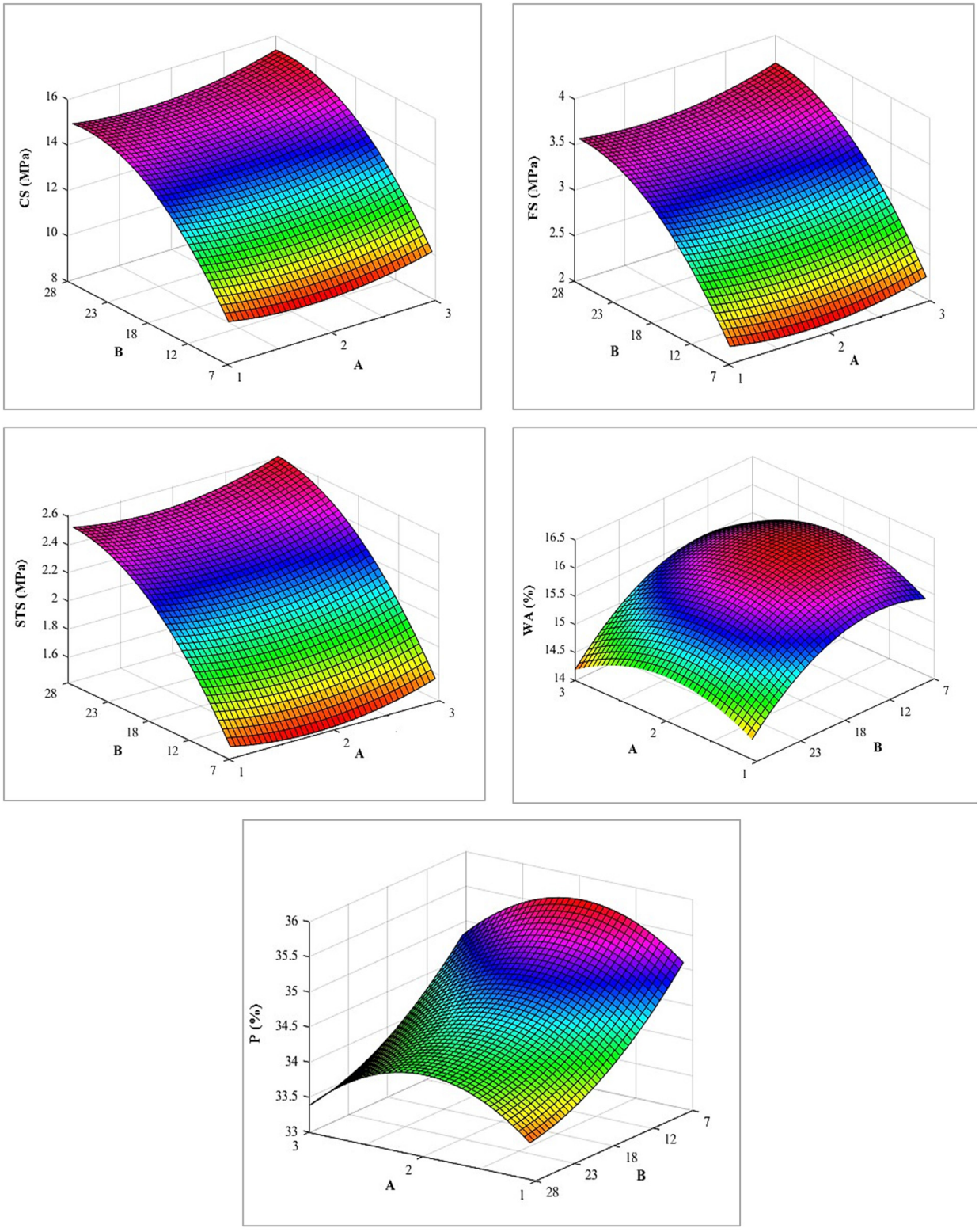

(a)

Figure 3: 3D response surfaces for CS, FS, STS, WA, and *P*: (a) additive type and curing time, (b) additive type and additive content, and (c) curing time and additive content.

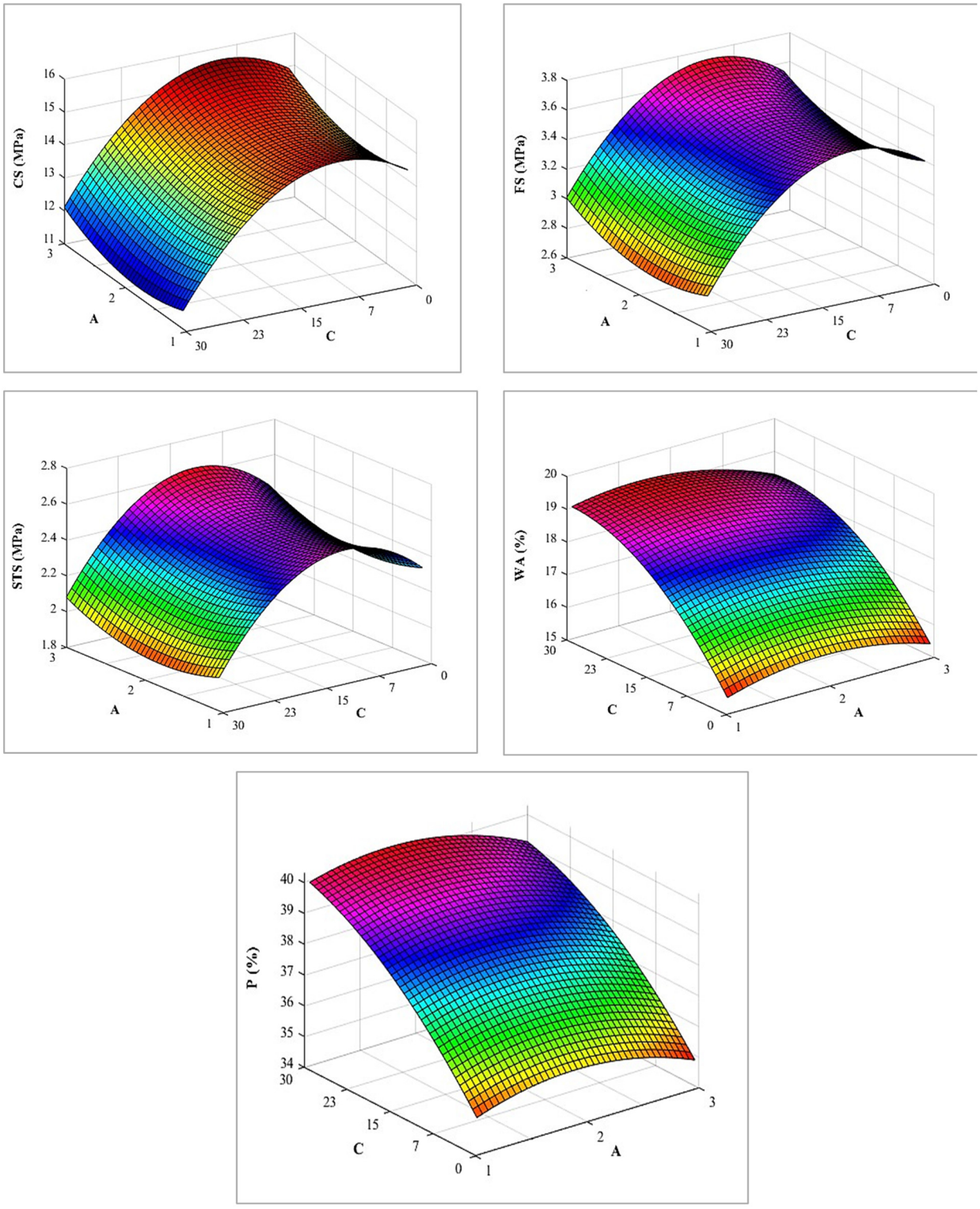

(b)

Figure 3: (*Continued*)

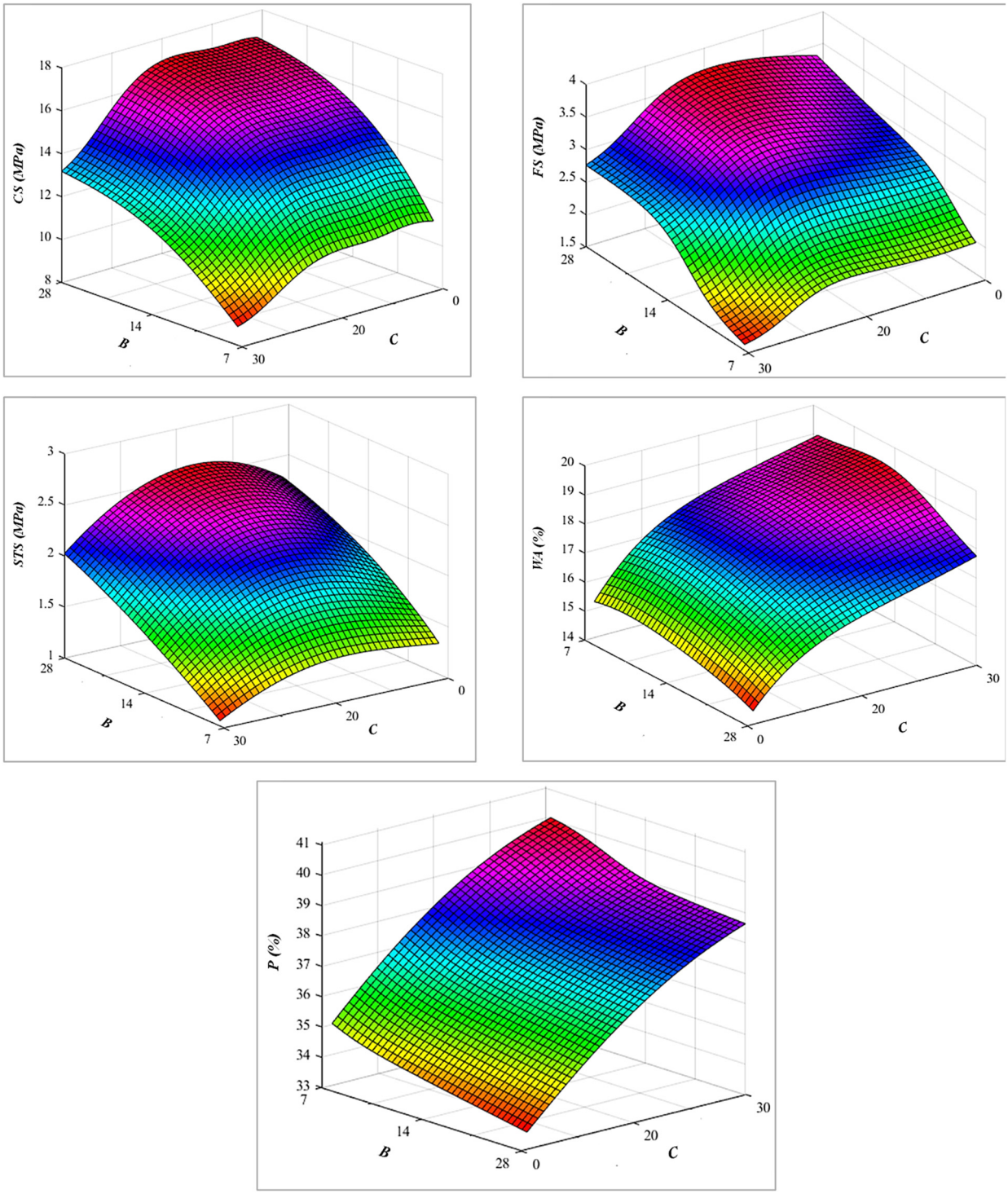

(c)

Figure 3: (*Continued*)

Table 3 presents the ANOVA of LFC properties with the variation in three factors: additive type (*A*), curing time (*B*), and additive content (*C*).

The contribution of curing time (*B*), which achieved 71.20, 77.89, and 78.06%, is more significant than that of additive content (*C*), with 10.29, 7.12, and 5.02% in CS, FS, and STS, respectively. Additive type (*A*) is deemed insignificant (*P* value >0.05) for CS, FS, and STS. Notably, the significance of additive content (*C*) with 63.63 and 79.78% is more pronounced than that of curing time (*B*) with 18.34 and 10.42%, as well as that of additive type (*A*) with 1.86 and 1.40% for WA and P, respectively.

The perturbation diagram of the obtained models is illustrated in Figure 1. The perturbation diagram serves as a graphical tool frequently utilized in engineering to illustrate the impact of various factors on the output of interest. This process assists in identifying and analyzing the impact of variations or disturbances in input variables on the overall output. The diagram illustrates that the input variables have been normalized and are displayed on a scale ranging from −1 to +1 [52]. This normalization allows for easier comparison and analysis of the input-output relationships, regardless of the original units or scales of the variables. The diagram illustrates how the system's output responds to simultaneous changes in the three normalized inputs, helping to pinpoint the input combinations that have the most significant impact on the output, as well as potential interactions among the variables.

Figure 1(a)–(c) illustrate an increase in the CS, FS, and STS parameters as the *B* factor positively increases (level +1), while an increase in the *C* factor occurs near the reference point on the negative side (level −1). In addition, factor A shows a slight increase on both the positive side (level +1) and the negative side (level −1). Figure 1(d) reveals a significant increase in the value of WA with the elevation of factor C on the right side (level +1), while *A* and *B* increase near the reference point on the left side (level −1). In Figure 1(e), an increase in the value of *P* is observed with the increase in factor *B* on the left side (level −1) and factor *C* on the right side (level +1), while *A* increases near the reference point on the left side (level −1) (Figure 2).

With a significance level of $\alpha = 0.05$, the *p*-values for all outputs presented in Table 4 exceed this threshold, indicating that we fail to reject the null hypothesis in every case. Consequently, the residuals for each output can be considered to follow a normal distribution.

4.2 3D response surfaces

The 3D surface response plots illustrate the impact of variables such as additive type, curing time, and additive content (noted *A*, *B*, and *C*, respectively) on the properties of CS, FS, STS, WA, and *P*, as depicted in Figure 3(a)–(c).

In the 3D response surface plots, color coding is used to visually represent the effect of varying input variables, such as additive type, curing time, and additive content, on the physicomechanical properties of LFC. The plots help to illustrate how these variables interact to influence outcomes like CS or FS.

The color scheme in the plots provides a clear visual guide, with pink areas indicating regions of highest response intensity, where the desired property (such as CS) is maximized. Conversely, red areas represent regions of lowest response intensity, indicating weaker performance in the property being measured. For example, a high CS may occur in the pink areas when the curing

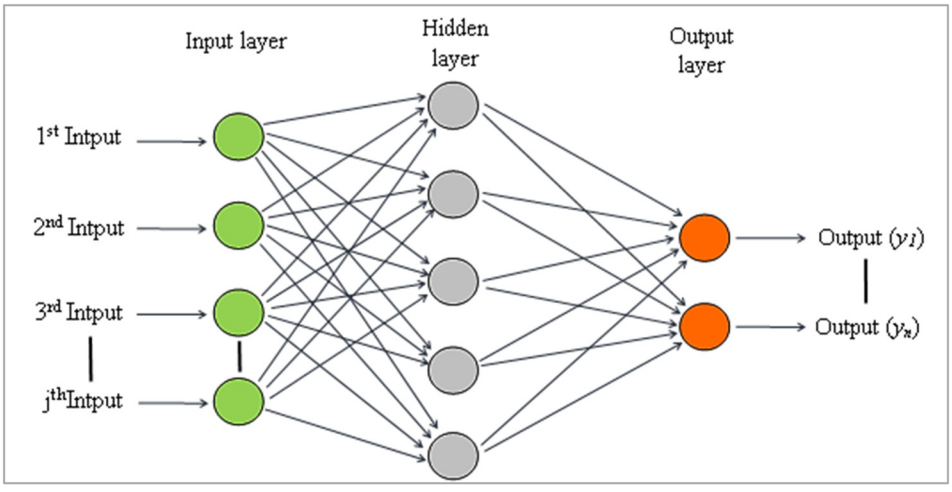

Figure 4: Graphical representation of an ANN perceptron.

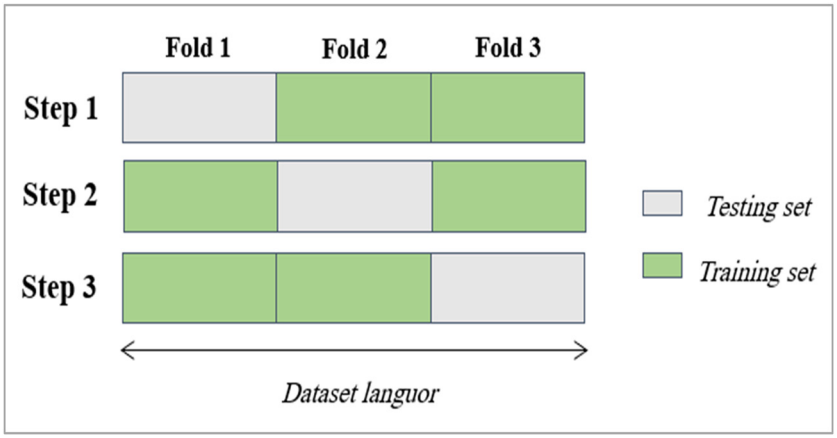

Figure 5: Schematic representation of *K*-fold cross-validation [71].

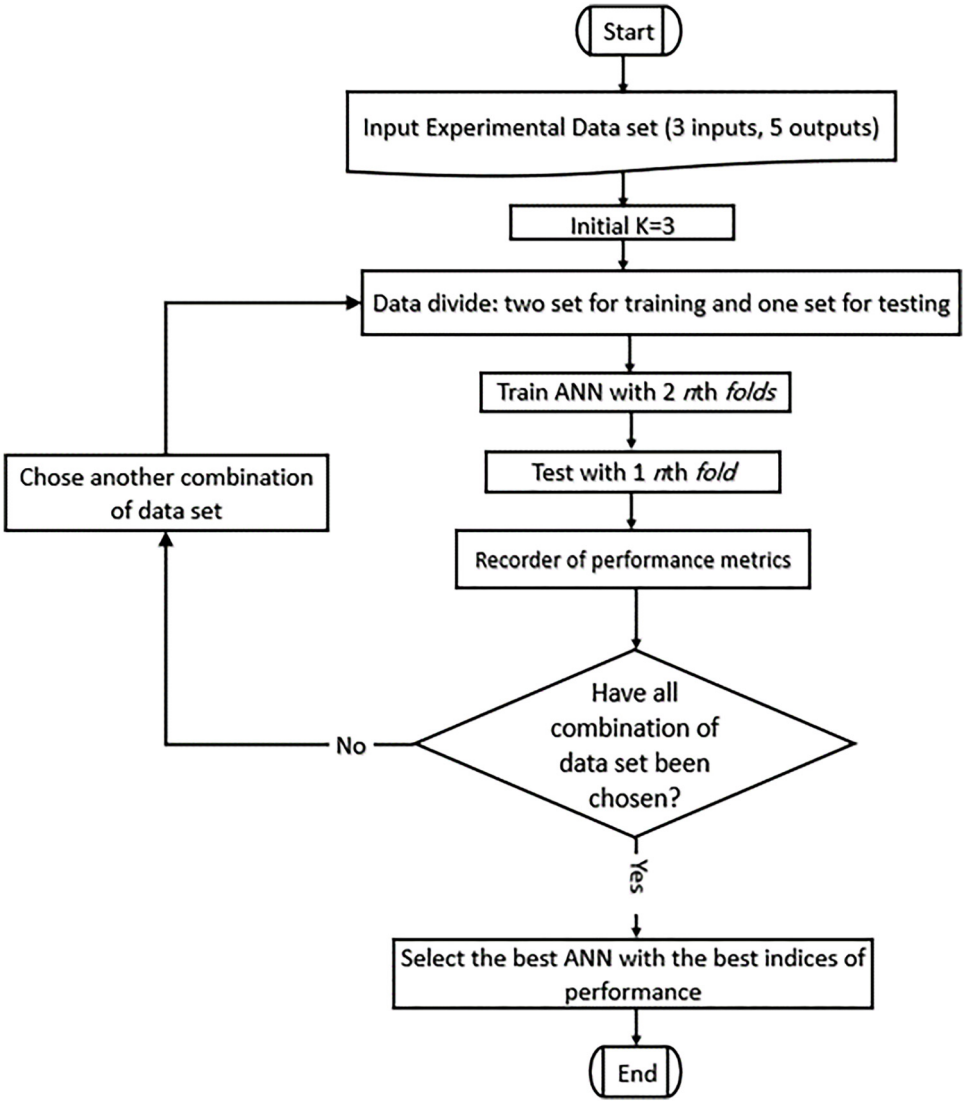

Figure 6: Flowchart of the *K*-fold cross-validation.

Table 5: Optimal architectures of ANN

ANN model	Number of hidden layers			Activation functions
CS	2	The first layer: 6 nodes	3	Sigmoïde
			2	Linear
			1	Gaussian
		The second layer: 4 nodes	2	Sigmoïde
			1	Linear
			1	Gaussian
FS	1	4 nodes		Sigmoïde
STS	1	4 nodes		Sigmoïde
WA	1	6 nodes		Sigmoïde
P	1	5 nodes	3	Sigmoïde
			2	Linear

time is 28 days and the additive content is 20%, while the red areas might indicate poor results when the curing time is shorter or the additive content is lower.

The substitution of cement with three types of additives, namely, OSA, SSA and MSA, with a curing time of 28 days and an additive concentration ranging from 4 to 20%, results in maximum mechanical strength, whether in terms of compression, flexion or splitting tensile strength, for the LFC.

After a curing period of 28 days and an additive concentration fluctuating between 18 and 30%, MSA displays a lower WA capacity compared with samples containing OSA and SSA in the LFC.

Following a curing period of 28 days and an additive concentration ranging from 24 to 30%, OSA and MSA ashes exhibit lower *P* than the sample containing SSA ash in the LFC.

5 Predictive modeling

5.1 ANN *K*-fold cross validation modeling

The human brain comprises a vast network of neurons connected by synapses. When an individual interacts with their environment, such as through sight or hearing, specific neurons are activated [65,66]. This activation enables the person to distinguish between various stimuli. ANNs aim to replicate this process [67,68].

ANNs are organized in layers to successively analyze input. The input layer acquires raw data and transmits it to the following levels. Hidden layers, situated between input

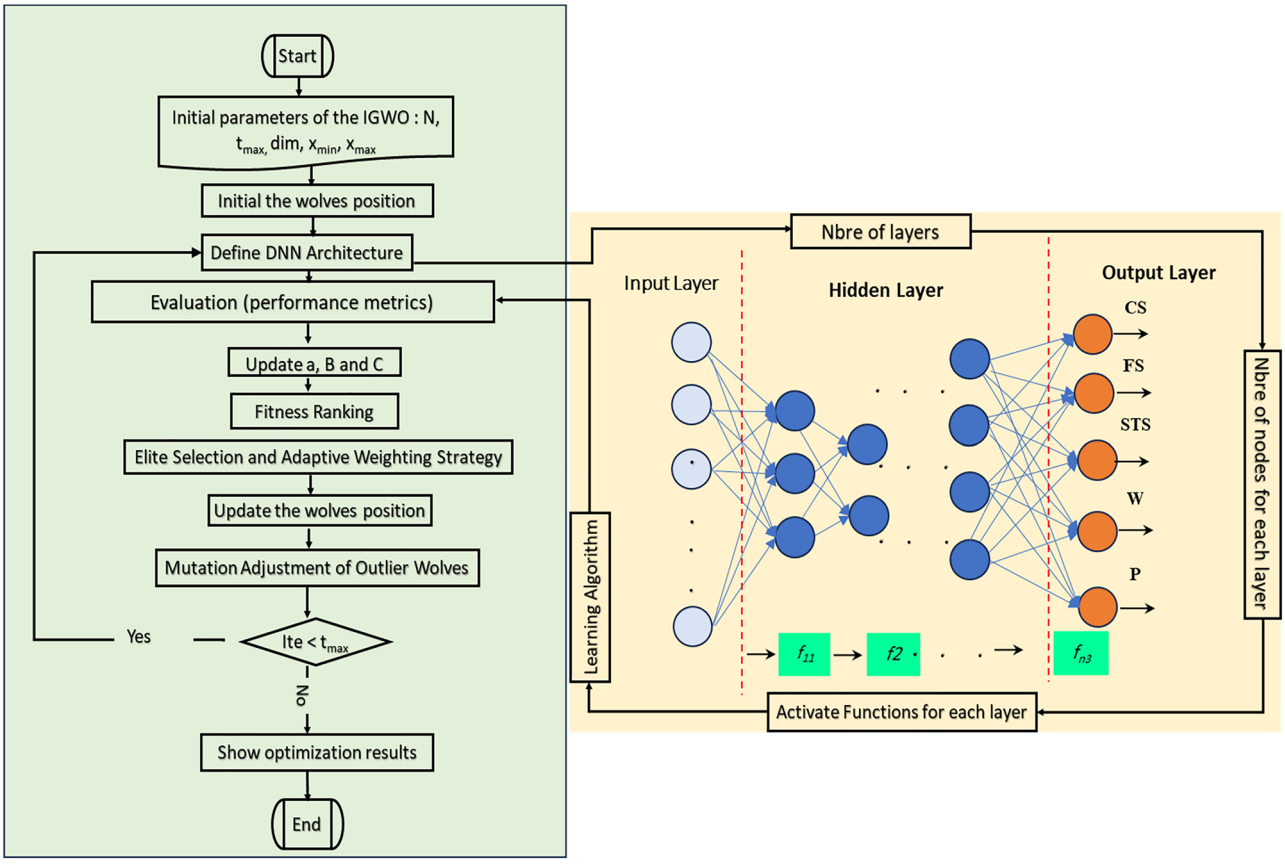

Figure 7: Flow chart of the hybrid algorithm DNN-IGWO.

Table 6: DNN optimization parameters

Hidden layers	Hidden layer size	Learning algorithms	Activation functions
Min: 1 Max: 10	Min: 1 Max: 10	Trainlm: LM backpropagation Trainbr: Bayesian regulation backpropagation Trainbfg: BFGS quasi-Newton backpropagation Traincgb: Conjugate gradient backpropagation with Powell-Beale restarts Traincgf: Conjugate gradient backpropagation with Fletcher-Reeves updates Traincgp: Conjugate gradient backpropagation with Polak-Ribiere updates Traingd: Gradient descent backpropagation Traingda: Gradient descent with adaptive lr backpropagation Traingdm: Gradient descent with momentum Traingdx: Gradient descent w/momentum and adaptive lr backpropagation Trainoss: One step secant backpropagation Trainrp: RPROP backpropagation Trainscg: Scaled conjugate gradient backpropagation	Compet: Competitive transfer function Elliotsig: Elliot sigmoid transfer function Hardlim: Positive hard limit transfer function Hardlims: Symmetric hard limit transfer function Logsig: Logarithmic sigmoid transfer function Netinv: Inverse transfer function Poslin: Positive linear transfer function Purelin: Linear transfer function Radbas: Radial basis transfer function Radbasn: Radial basis normalized transfer function Satlin: Positive saturating linear transfer function Satlins: Symmetric saturating linear transfer function Softmax: Soft max transfer function Tansig: Symmetric sigmoid transfer function Tribas: Triangular basis transfer function

and output, execute computations by using weights, biases, and activation functions (*e.g.*, ReLU, sigmoid) to convert data into significant patterns [69,70]. These layers facilitate the network's ability to comprehend intricate relationships – an increased number of hidden layers permits more profound feature extraction, being the foundation of "deep learning." The output layer generates the outcome, such as a classification or numerical prediction, utilizing task-specific activations like softmax or linear functions. Collectively, these layers emulate hierarchical information processing, transforming raw inputs into useful insights [72,73]. This architecture is an ANN perceptron, as shown in Figure 4.

Supposing a neural network with N layers, we define the following quantities:

$$y_j^n = \sum_k w_{jk} a_k^{n-1} + b_j^n; \quad \forall N = 1, \ldots, n-1, n, \tag{13}$$

$$a_j^n = f\left(\sum_k w_{jk} a_k^{n-1} + b_j^n\right) = f(y_j^n); \quad \forall N = 1, \ldots, n-1, n, \tag{14}$$

Table 7: Optimal parameters of DNN obtained with IGWO

Parameter	HLayer number	HLayer size	Learning-algorithm	Act-Fct
CS	3	9	Trainbr	Logsig
		8		Elliotsig
		9		Elliotsig
FS	3	10	Trainbr	Elliotsig
		8		Tansig
		5		Radbasn
STS	2	8	Trainbr	Elliotsig
		9		Radbasn
WA	2	8	Trainbr	Elliotsig
		8		Logsig
P	2	9	Trainbr	Elliotsig
		8		Radbasn

Table 8: Error functions [80]

Criteria	Formulas
RMSE	$\sum_{x=1}^{n} \sqrt{\frac{(y_{ex} - y_{px})^2}{n}}$
MAPE (%)	$\sum_{x=1}^{n} \frac{\lvert (y_{ex} - y_{px})/y_{ex} \rvert}{n} \times 100$
MAD	$\sum_{x=1}^{n} \frac{\lvert (y_{ex} - y_{px}) \rvert}{n}$
R^2	$\frac{\sum_{x=1}^{n}(y_{px} - y_{ex})}{\sum_{x=1}^{n}(y_{px} - \bar{y})^2}$
OBJ	$\frac{\mathrm{RMSE} + \mathrm{MAE}}{R^2 + 1}$

where y_{ex} represents the experimental value of the xth trial.
y_{px} denotes the predicted value of the xth trial.
$\overline{y}$ denotes the average of the experimentally determined values.
n represents the number of experiments.

Table 9: Experimental and predictive CS results

N	FS Exp. (MPa)	FS RSM (MPa)	FS ANN (MPa)	FS DNN (MPa)	FS SVM (MPa)
1	2.10	1.99	2.07	2.10	2.35
2	2.80	2.78	2.81	2.80	2.79
3	3.40	3.43	3.35	3.40	3.67
4	2.00	2.14	2.06	2.00	2.26
5	2.90	2.93	2.87	2.90	2.70
6	3.50	3.56	3.52	3.50	3.58
7	2.10	2.20	2.08	2.10	2.17
8	2.90	2.98	2.95	2.90	2.61
9	3.60	3.60	3.63	3.60	3.48
10	2.20	2.16	2.13	2.20	2.07
11	3.00	2.94	3.01	3.00	2.51
12	3.70	3.55	3.66	3.70	3.39
13	2.00	2.03	2.07	2.00	1.98
14	2.80	2.80	2.90	2.80	2.42
15	3.50	3.40	3.50	3.50	3.30
16	1.80	1.81	1.81	1.72	1.89
17	2.50	2.57	2.50	2.50	2.33
18	3.10	3.16	3.08	3.10	3.20
19	1.60	1.50	1.59	1.60	1.79
20	2.30	2.25	2.14	2.30	2.23
21	2.80	2.83	2.76	2.80	3.11
22	2.10	1.88	2.07	2.10	2.43
23	2.80	2.69	2.78	2.80	2.87
24	3.40	3.35	3.27	3.40	3.75
25	2.00	2.04	2.04	2.00	2.34
26	2.80	2.84	2.83	2.80	2.78
27	3.40	3.49	3.44	3.40	3.66
28	2.00	2.10	2.05	2.00	2.25
29	2.80	2.89	2.89	2.80	2.68
30	3.50	3.54	3.57	3.50	3.56
31	2.10	2.07	2.05	2.02	2.15
32	2.90	2.86	2.92	2.90	2.59
33	3.60	3.49	3.60	3.75	3.47
34	1.90	1.95	1.93	1.90	2.06
35	2.70	2.73	2.78	2.74	2.50
36	3.40	3.35	3.41	3.40	3.38
37	1.70	1.73	1.64	1.70	1.97
38	2.50	2.50	2.38	2.50	2.41
39	3.00	3.11	2.99	3.00	3.28
40	1.50	1.42	1.49	1.50	1.87
41	2.20	2.19	2.10	2.20	2.31
42	2.70	2.79	2.72	2.70	3.19
43	2.10	2.04	2.10	2.10	2.51
44	2.80	2.85	2.82	2.80	2.95
45	3.40	3.54	3.41	3.40	3.83
46	2.10	2.20	2.12	2.10	2.42
47	3.00	3.01	2.96	3.00	2.86
48	3.60	3.69	3.66	3.60	3.73
49	2.20	2.27	2.22	2.20	2.32
50	3.10	3.07	3.11	3.10	2.76
51	3.80	3.74	3.83	3.80	3.64
52	2.30	2.24	2.28	2.30	2.23
53	3.20	3.04	3.16	3.20	2.67
54	4.00	3.69	3.86	4.00	3.55
55	2.10	2.12	2.11	2.10	2.14
56	2.90	2.91	2.97	2.93	2.58
57	3.60	3.56	3.64	3.60	3.46
58	1.80	1.91	1.81	1.80	2.05
59	2.60	2.70	2.60	2.60	2.48
60	3.20	3.33	3.23	3.20	3.36
61	1.70	1.60	1.72	1.70	1.95
62	2.40	2.38	2.39	2.39	2.39
63	3.00	3.01	3.02	3.00	3.27

(*Continued*)

Table 9: *Continued*

where y is the output variable to be modeled. $a_j^0 = x_j$; x_j is the jth input layer; and w_{jk}^n is the weight value of the kth neuron in the nth layer at the jth neuron in the $(n-1)$th layer. Similarly, we define the biases b_i^j and the activation function f.

After an ANN model is trained on labeled data, its performance needs to be verified on new data. A critical step – model validation – is performed to ensure the accuracy of the prediction model. This process entails assessing whether the predicted results, which quantify hypothetical relationships between variables, are acceptable as adequate representations of the data.

One of the commonly used methods to assess the effectiveness of an ANN model is K-fold cross-validation, which is a resampling method that allows a model to be evaluated even when data are limited [74,75]. K-fold is easy to understand and is highly popular. Compared with other cross-validation approaches, it generally tends to produce a less biased model [76,77]. This result occurs because K-fold ensures that all observations from the original dataset have the opportunity to appear in the training set and the test set simultaneously. In the case of limited input data, K-fold is thus one of the most relevant approaches [78].

The first step is to randomly divide the dataset into K folds. This procedure is governed by a single parameter called K, which represents the number of groups into which the sample will be partitioned [79]. The value of K must be chosen wisely based on the size of the dataset, avoiding it being too low or too high. In this case, $K = 3$, which means that the dataset will be segmented into three distinct parts. Subsequently, we proceed with an iterative learning process, where we train the model on one-fold and test it on the others. This process repeats until each K-fold has been used in the training set at least once (Figure 5). The model's performance metric is evaluated

Table 10: Experimental and predictive FS results

N	STS Exp. (MPa)	STS RSM (MPa)	STS ANN (MPa)	STS DNN (MPa)	STS SVM (MPa)
1	15.54	15.42	15.34	15.54	16.47
2	15.22	15.60	15.45	15.22	16.01
3	14.50	14.36	14.47	14.50	15.10
4	16.80	16.51	16.74	16.66	16.99
5	16.91	16.67	16.87	16.91	16.54
6	15.60	15.40	15.65	15.61	15.62
7	17.57	17.40	17.59	17.57	17.52
8	17.76	17.55	17.75	17.76	17.06
9	16.30	16.25	16.33	16.30	16.14
10	18.08	18.10	18.08	18.08	18.04
11	18.25	18.23	18.30	18.26	17.58
12	16.75	16.90	16.76	16.75	16.66
13	18.46	18.60	18.43	18.45	18.56
14	18.65	18.72	18.69	18.65	18.10
15	17.10	17.36	17.09	17.10	17.19
16	18.74	18.91	18.73	18.74	19.09
17	18.95	19.02	19.00	18.97	18.63
18	17.40	17.63	17.40	17.40	17.71
19	18.97	19.03	19.03	18.98	19.61
20	19.25	19.12	19.26	19.25	19.15
21	17.70	17.71	17.75	17.70	18.23
22	15.54	15.90	15.45	15.54	16.20
23	15.22	16.06	15.36	15.22	15.74
24	14.50	14.78	14.65	14.50	14.82
25	17.06	16.93	16.99	17.09	16.72
26	17.23	17.08	16.91	17.23	16.26
27	15.90	15.77	15.90	15.83	15.35
28	17.88	17.77	17.92	17.88	17.25
29	18.03	17.90	17.90	18.03	16.79
30	16.70	16.56	16.66	16.70	15.87
31	18.36	18.41	18.47	18.37	17.77
32	18.53	18.53	18.52	18.53	17.31
33	17.20	17.16	17.17	17.20	16.39
34	18.76	18.86	18.81	18.75	18.29
35	18.93	18.96	18.95	18.92	17.83
36	17.60	17.57	17.56	17.59	16.92
37	19.05	19.12	19.07	19.04	18.81
38	19.23	19.21	19.25	19.25	18.36
39	17.90	17.78	17.91	17.91	17.44
40	19.27	19.18	19.27	19.28	19.34
41	19.53	19.25	19.45	19.52	18.88
42	18.20	17.80	18.24	18.19	17.96
43	15.54	15.36	15.14	15.54	15.93
44	15.22	15.50	15.30	15.22	15.47
45	14.50	14.18	14.39	14.50	14.55
46	16.61	16.33	16.46	16.61	16.45
47	16.63	16.46	16.59	16.63	15.99
48	15.20	15.12	15.32	15.20	15.07
49	17.21	17.11	17.22	17.21	16.97
50	17.43	17.23	17.37	17.43	16.52
51	15.80	15.86	15.84	15.80	15.60
52	17.61	17.70	17.65	17.62	17.50
53	17.83	17.80	17.84	17.84	17.04
54	16.20	16.40	16.16	16.21	16.12
55	17.91	18.10	17.91	17.90	18.02
56	18.13	18.18	18.15	18.12	17.56
57	16.50	16.75	16.42	16.48	16.64
58	18.11	18.30	18.10	18.12	18.54
59	18.33	18.37	18.38	18.34	18.08
60	16.70	16.91	16.67	16.71	17.17
61	18.31	18.31	18.28	18.31	19.07
62	18.53	18.36	18.53	18.53	18.61
63	16.90	16.88	16.93	16.90	17.69

by taking the average of the recorded scores [81,82]. Figure 6 illustrates the flowchart of the *K*-fold cross-validation process employed in training the ANN model.

The architecture of an ANN defines how neurons are structured in layers and connected to each other [83,84]. The parameters optimized in this section include the size of the network, which encompasses the number of hidden layers and the number of nodes in each layer, as well as the activation functions for each layer [84,85]. The dimension of the network is particularly important when designing a neural network, as it determines the number of layers and nodes in each of them. Activation functions influence the output of a neuron based on its inputs. In this study, three types of activation functions were evaluated: the sigmoid transfer function (hyperbolic tangent), the linear transfer function, and the radial basis function (Gaussian) [86,87]. The optimal architectures of ANNs, aiming to maximize the performance of prediction models for CS, FS, STS, WA, and *P*, are presented in Table 5.

ANN-K fold validation models with different architectures have been developed.

5.2 Hybrid deep neural network optimization using improved grey wolf optimizer (DNN-IGWO)

Figure 7 depicts the architecture of the DNN-IGWO, which represents an advanced hybrid modeling strategy developed to improve both the predictive performance and computational robustness of the learning process. By integrating the deep representation learning strengths of DNNs with the metaheuristic optimization capabilities of the IGWO algorithm, this approach enables the automated configuration of network design parameters and

Table 11: Experimental and predictive STS results

N	CS Exp. (MPa)	CS RSM (MPa)	CS ANN (MPa)	CS DNN (MPa)	CS SVM (MPa)
1	9.2	8.86	9.19	2.1	1.99
2	12.2	12.08	12.44	2.8	2.78
3	14.5	14.47	14.54	3.4	3.43
4	9.3	9.56	9.20	2	2.14
5	12.5	12.72	12.58	2.9	2.93
6	14.7	15.01	14.93	3.5	3.56
7	9.5	9.85	9.50	2.1	2.20
8	12.7	12.96	12.92	2.9	2.98
9	15.0	15.14	15.38	3.6	3.60
10	9.8	9.73	9.62	2.2	2.16
11	13.1	12.79	12.94	3	2.94
12	15.4	14.86	15.37	3.7	3.55
13	9.0	9.20	9.17	2	2.03
14	12.2	12.21	12.23	2.8	2.80
15	14.2	14.17	14.51	3.5	3.40
16	8.3	8.27	8.26	1.80	1.81
17	11	11.22	10.85	2.5	2.57
18	13.0	13.08	12.92	3.1	3.16
19	7.3	6.92	7.81	1.6	1.50
20	9.9	9.82	9.83	2.30	2.25
21	11.7	11.58	11.72	2.80	2.83
22	9.2	8.51	8.99	2.10	1.88
23	12.2	11.76	12.26	2.80	2.69
24	14.5	14.20	14.37	3.4	3.35
25	9.10	9.21	9.22	2	2.04
26	12.3	12.41	12.49	2.8	2.84
27	14.5	14.74	14.56	3.4	3.49
28	9.10	9.51	8.99	2	2.10
29	12.4	12.65	12.34	2.8	2.89
30	14.6	14.88	14.62	3.5	3.54
31	9.4	9.39	8.91	2.1	2.07
32	12.7	12.48	12.32	2.9	2.86
33	14.9	14.60	14.73	3.6	3.49
34	8.8	8.87	8.57	1.9	1.95
35	11.9	11.91	11.83	2.7	2.73
36	14.1	13.92	14.19	3.4	3.35
37	7.9	7.94	7.65	1.7	1.73
38	10.6	10.92	10.53	2.5	2.50
39	12.6	12.83	12.71	3	3.11
40	6.9	6.60	6.91	1.50	1.42
41	9.4	9.53	9.18	2.20	2.19
42	11.1	11.33	11.18	2.70	2.79
43	9.2	9.17	9.05	2.10	2.04
44	12.2	12.44	12.19	2.80	2.85
45	14.5	14.94	14.28	3.40	3.54
46	9.5	9.88	9.67	2.10	2.20
47	12.9	13.10	12.96	3	3.01
48	15.1	15.49	15.17	3.60	3.69
49	10.1	10.18	10.18	2.20	2.27
50	13.6	13.34	13.58	3.10	3.07
51	15.9	15.63	15.86	3.80	3.74
52	10.3	10.07	10.31	2.30	2.24
53	14.0	13.18	13.70	3.2	3.04
54	16.3	15.36	15.89	4	3.69
55	9.4	9.55	9.47	2.1	2.12
56	12.7	12.61	12.76	2.9	2.91
57	14.9	14.68	14.98	3.6	3.56
58	8.3	8.63	8.31	1.8	1.91
59	11.2	11.63	11.36	2.6	2.70
60	13.1	13.60	13.61	3.2	3.33
61	7.6	7.29	7.56	1.7	1.60
62	10.3	10.24	9.93	2.4	2.38
63	12.0	12.10	11.96	3	3.01

(*Continued*)

hyperparameters [88–90]. The central aim of this framework is to enhance the prediction accuracy of mechanical properties through the systematic optimization of critical model components, including the number and depth of hidden layers, the distribution of neurons, and the activation function types.

At the outset of the optimization process, the parameters of the IGWO are initialized, these include the number of search agents, the dimensionality of the problem space, and the maximum iteration count. These parameters critically influence the convergence behavior of the algorithm by regulating the dynamics of the exploration and exploitation mechanisms. Upon initialization, the structure of the DNN is constructed, detailing the number of layers and the specific configuration of neurons per layer, which will subsequently be optimized through the IGWO process.

The optimization process is focused on determining the optimal number of hidden layers, neurons per layer, activation functions, and learning algorithms. Unlike conventional methods, IGWO enabled an automated and efficient search for the best-performing DNN configuration, improving predictive accuracy and generalization. The learning algorithms evaluated included trainlm, trainbr, trainbfg, and others, while multiple activation functions were considered to ensure adaptability to nonlinear patterns. Table 6 details the optimized architecture of DNN.

The Levenberg–Marquardt (LM) optimizer was selected for training the ANN because of its swift convergence and stability, making it particularly appropriate for small to medium-sized datasets such as the one utilized in this study. The LM algorithm integrates the benefits of gradient descent and the Gauss-Newton method, facilitating rapid training while addressing the intricate nonlinear interactions within the dataset [91,92]. Its adaptability in managing both linear and nonlinear models renders it optimum for forecasting

Table 12: Experimental and predictive WA results

N	WA Exp. (%)	WA RSM (%)	WA ANN (%)	WA DNN (%)	WA SVM (%)
1	15.54	15.42	15.34	15.54	16.47
2	15.22	15.60	15.45	15.22	16.01
3	14.50	14.36	14.47	14.50	15.10
4	16.80	16.51	16.74	16.66	16.99
5	16.91	16.67	16.87	16.91	16.54
6	15.60	15.40	15.65	15.61	15.62
7	17.57	17.40	17.59	17.57	17.52
8	17.76	17.55	17.75	17.76	17.06
9	16.30	16.25	16.33	16.30	16.14
10	18.08	18.10	18.08	18.08	18.04
11	18.25	18.23	18.30	18.26	17.58
12	16.75	16.90	16.76	16.75	16.66
13	18.46	18.60	18.43	18.45	18.56
14	18.65	18.72	18.69	18.65	18.10
15	17.10	17.36	17.09	17.10	17.19
16	18.74	18.91	18.73	18.74	19.09
17	18.95	19.02	19.00	18.97	18.63
18	17.40	17.63	17.40	17.40	17.71
19	18.97	19.03	19.03	18.98	19.61
20	19.25	19.12	19.26	19.25	19.15
21	17.70	17.71	17.75	17.70	18.23
22	15.54	15.90	15.45	15.54	16.20
23	15.22	16.06	15.36	15.22	15.74
24	14.50	14.78	14.65	14.50	14.82
25	17.06	16.93	16.99	17.09	16.72
26	17.23	17.08	16.91	17.23	16.26
27	15.90	15.77	15.90	15.83	15.35
28	17.88	17.77	17.92	17.88	17.25
29	18.03	17.90	17.90	18.03	16.79
30	16.70	16.56	16.66	16.70	15.87
31	18.36	18.41	18.47	18.37	17.77
32	18.53	18.53	18.52	18.53	17.31
33	17.20	17.16	17.17	17.20	16.39
34	18.76	18.86	18.81	18.75	18.29
35	18.93	18.96	18.95	18.92	17.83
36	17.60	17.57	17.56	17.59	16.92
37	19.05	19.12	19.07	19.04	18.81
38	19.23	19.21	19.25	19.25	18.36
39	17.90	17.78	17.91	17.91	17.44
40	19.27	19.18	19.27	19.28	19.34
41	19.53	19.25	19.45	19.52	18.88
42	18.20	17.80	18.24	18.19	17.96
43	15.54	15.36	15.14	15.54	15.93
44	15.22	15.50	15.30	15.22	15.47
45	14.50	14.18	14.39	14.50	14.55
46	16.61	16.33	16.46	16.61	16.45
47	16.63	16.46	16.59	16.63	15.99
48	15.20	15.12	15.32	15.20	15.07
49	17.21	17.11	17.22	17.21	16.97
50	17.43	17.23	17.37	17.43	16.52
51	15.80	15.86	15.84	15.80	15.60
52	17.61	17.70	17.65	17.62	17.50
53	17.83	17.80	17.84	17.84	17.04
54	16.20	16.40	16.16	16.21	16.12
55	17.91	18.10	17.91	17.90	18.02
56	18.13	18.18	18.15	18.12	17.56
57	16.50	16.75	16.42	16.48	16.64
58	18.11	18.30	18.10	18.12	18.54
59	18.33	18.37	18.38	18.34	18.08
60	16.70	16.91	16.67	16.71	17.17
61	18.31	18.31	18.28	18.31	19.07
62	18.53	18.36	18.53	18.53	18.61
63	16.90	16.88	16.93	16.90	17.69

the physicomechanical properties of concrete, ensuring an ideal equilibrium between computing efficiency and model precision.

The optimization of DNN architectures through the IGWO has led to the development of a bespoke model tailored for the prediction of five key mechanical and physical properties of concrete: CS, FS, STS, WA, and *P*. The optimized architecture, whose detailed configuration is presented in Table 7, includes essential design elements such as the number of hidden layers, neurons per layer, activation functions, and the selected learning algorithm.

5.3 Support vector machines (SVMs)

SVMs are a machine learning technique used for classification and regression. This method is based on the Vapnik-Chervonenkis statistical learning theory [93–95]. In 1995, Cortes and Vapnik [96] proposed an adaptation of SVMs to solve regression problems, using the kernel trick. This approach is essential in machine learning because it allows nonlinear problems to be addressed using linear classifiers in a transformed space.

Unlike ANNs, SVMs are capable of providing reliable predictions even with limited data and are less susceptible to overfitting [97]. For example, Ulas and Sami demonstrated the effectiveness of SVMs in predicting surface roughness during turning of AISI 304 steel, despite a small amount of experimental data [98].

5.4 Predictive modeling results

In this section, we trained, tested, and validated the different models of RSM, ANN, DNN-IGWO, and SVM to predict C, FS, STS, WA, and *P* using the 63 experimentally obtained

Table 13: Experimental and predictive *P* results

N	*P* Exp. (%)	*P* RSM (%)	*P* ANN (%)	*P* DNN (%)	*P* SVM (%)
1	35.10	35.12	35.12	35.10	35.49
2	34.40	34.33	34.42	34.40	35.06
3	33.70	33.53	33.58	33.70	34.20
4	36.50	36.32	36.32	36.48	36.33
5	35.60	35.55	35.54	35.62	35.90
6	34.90	34.77	34.74	34.90	35.05
7	37.50	37.36	37.40	37.52	37.17
8	36.70	36.60	36.54	36.67	36.74
9	35.90	35.85	35.80	35.91	35.89
10	38.30	38.25	38.32	38.29	38.02
11	37.50	37.50	37.41	37.52	37.59
12	36.70	36.77	36.73	36.69	36.73
13	38.90	38.97	39.07	38.87	38.86
14	38.20	38.24	38.16	38.21	38.43
15	37.40	37.54	37.51	37.41	37.57
16	39.30	39.54	39.65	39.33	39.70
17	38.80	38.82	38.80	38.78	39.27
18	38.10	38.15	38.14	38.10	38.42
19	39.70	39.96	40.08	39.69	40.54
20	39.20	39.25	39.34	39.21	40.11
21	38.60	38.60	38.63	38.60	39.26
22	35.10	35.69	35.04	35.42	35.29
23	34.40	34.93	34.42	34.40	34.86
24	33.70	34.17	33.76	33.70	34.00
25	36.70	36.84	36.81	36.70	36.13
26	36.10	36.09	36.08	36.09	35.70
27	35.20	35.36	35.42	35.20	34.84
28	38.00	37.84	38.03	37.99	36.97
29	37.30	37.10	37.20	37.31	36.54
30	36.40	36.40	36.55	36.40	35.69
31	38.90	38.68	38.88	38.91	37.81
32	38.20	37.95	38.00	38.19	37.39
33	37.40	37.27	37.39	37.39	36.53
34	39.50	39.36	39.51	39.54	38.66
35	38.80	38.65	38.64	38.81	38.23
36	38.00	37.99	38.05	38.00	37.37
37	40.00	39.88	39.99	40.00	39.50
38	39.30	39.18	39.18	39.30	39.07
39	38.60	38.55	38.56	38.60	38.21
40	40.40	40.25	40.34	40.26	40.34
41	39.70	39.56	39.65	39.70	39.91
42	39.00	38.96	38.96	39.00	39.06
43	35.10	34.83	35.11	35.33	35.09
44	34.40	34.09	34.43	34.40	34.66
45	33.70	33.38	33.70	33.70	33.80
46	36.10	35.94	36.08	36.10	35.93
47	35.20	35.21	35.32	35.25	35.50
48	34.70	34.53	34.67	34.70	34.64
49	36.90	36.89	36.91	36.90	36.77
50	36.10	36.17	36.08	36.10	36.34
51	35.50	35.51	35.50	35.50	35.49
52	37.60	37.68	37.57	37.60	37.61
53	36.90	36.98	36.72	36.90	37.18
54	36.20	36.34	36.17	36.20	36.33
55	38.20	38.31	38.10	38.20	38.45
56	36.70	37.63	37.27	36.70	38.03
57	36.90	37.02	36.73	36.90	37.17
58	38.70	38.79	38.58	38.70	39.30
59	38.20	38.12	37.84	38.19	38.87
60	37.50	37.53	37.28	37.50	38.01
61	39.10	39.11	39.22	39.10	40.14
62	38.70	38.45	38.65	38.70	39.71
63	38.00	37.89	38.09	37.89	38.86

(*Continued*)

Table 13: *Continued*

data points. Various visualization tools, such as scatter plots and spider plots, were used, complementing the evaluation metrics such as correlation coefficient (R^2), objective function (OBJ), and error criteria (root mean square error (RMSE), mean absolute percentage error (MAPE), and mean absolute deviation (MAD)). We used Taylor diagrams to illustrate the data availability and performance of each model. We examined the predictive capabilities of the different models by comparing the model predictions with the corresponding experimental data. Table 8 provides the formulas for calculating the error criteria.

Tables 9–13 and the distribution plots in Figure 8 compare the predictions of C, FS, STS, WA, and *P* with the actual values for four prediction models: RSM, ANN, DNN-IGWO, and SVM. The points are represented by different symbols depending on the models, while the solid lines $y = x$ and the dashed lines (+10 and −10%) serve as a reference to evaluate the accuracy of the models.

These distribution plots show that the neural network-based models ANN and DNN-IGWO significantly outperform traditional RSM and SVM models in terms of predictive accuracy. DNN-IGWO performs best, with near-perfect predictions within the ±10% error band, followed by ANN. RSM models show moderate accuracy, with greater dispersion. Finally, SVM models are the least accurate, with predictions largely deviating from the actual values, which limits their reliability for this task.

Table 14 and the spider plots in Figure 9 present the comparative analysis of the predictive models (RSM, ANN, DNN, and SVM) applied to the five target outputs (C, FS, STS, WA, and *P*). This analysis highlights the superiority of DNN. For all outputs, the DNN model systematically presents the best performances with the lowest values of error indicators (MAD, RMSE, MAPE) and the highest coefficients of determination ($R^2 \approx 0.999$), reflecting remarkable accuracy and generalization capacity. Conversely, the SVM model is distinguished by the highest errors and the lowest R^2 values, particularly for the C, STS, WA, and *P* outputs, demonstrating a more limited predictive capacity. The RSM

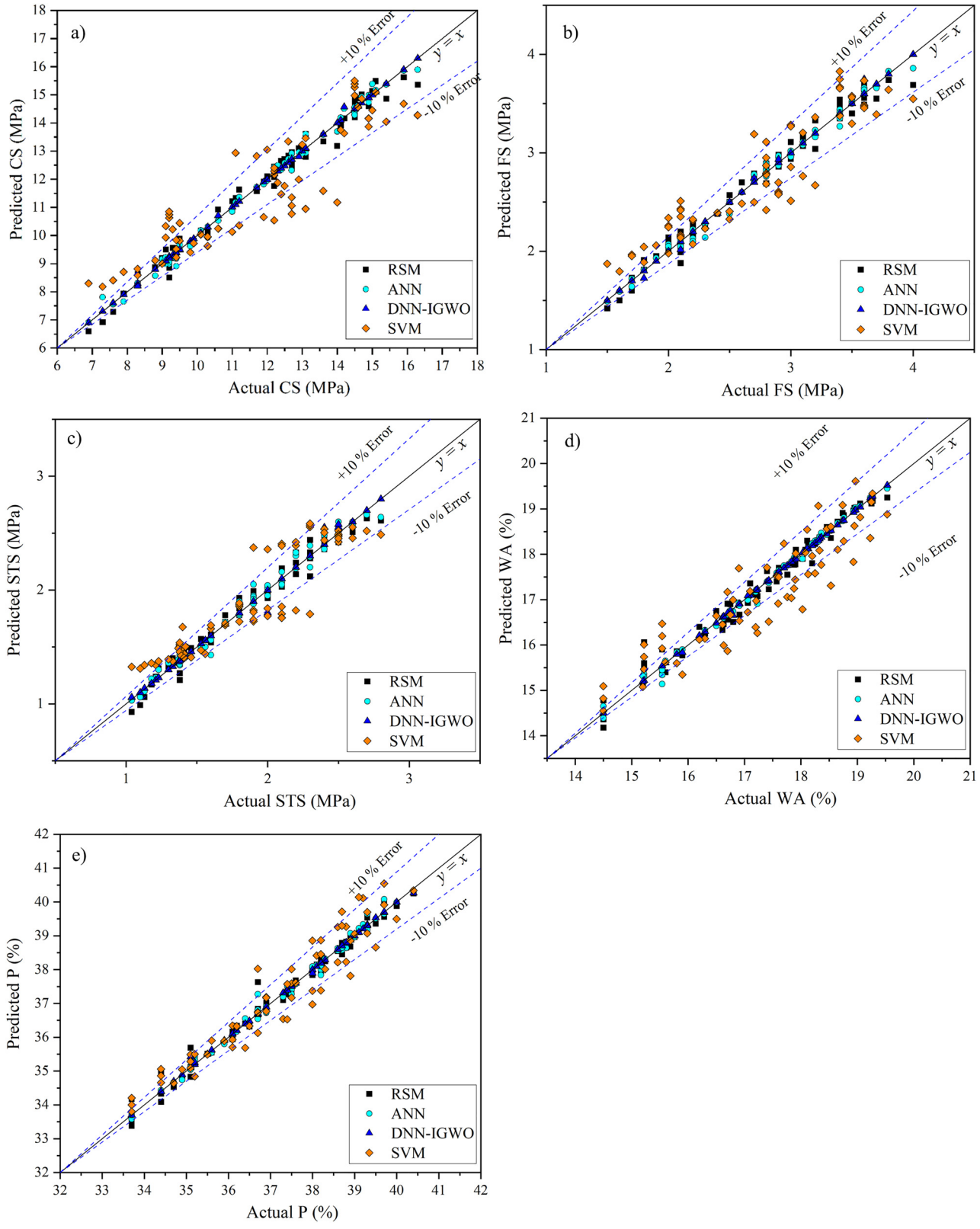

Figure 8: Comparison of measured values of (a) CS, (b) FS, (c) STS, (d) WA, and (e) *P* and predicted values using RSM, ANN, SNN-IGWO, and SVM models.

Table 14: Comparison between performance indices of RSM, ANN, IGWO, and SVM models

	CS				FS				STS				WA				P			
	RSM	ANN	DNN	SVM	RSM	ANN	DNN	SVM	RSM	ANN	DNN	SVM	RSM	ANN	DNN	SVM	RSM	ANN	DNN	SVM
MAD	0.245	0.144	0.016	0.839	0.069	0.039	0.006	0.208	0.059	0.045	0.008	0.158	0.155	0.060	0.009	0.454	0.143	0.097	0.021	0.417
RMSE	0.307	0.194	0.052	1.044	0.088	0.053	0.025	0.246	0.073	0.060	0.034	0.197	0.203	0.094	0.021	0.554	0.212	0.143	0.056	0.527
MAPE (%)	2.135	1.289	0.137	7.373	2.682	1.493	0.248	8.098	3.374	2.459	0.375	8.743	0.927	0.361	0.049	2.619	0.392	0.261	0.056	1.112
R^2	0.984	0.994	0.999	0.818	0.981	0.993	0.999	0.853	0.976	0.984	0.995	0.826	0.976	0.995	0.999	0.838	0.985	0.993	0.999	0.914
OBJ	0.278	0.169	0.034	1.036	0.079	0.046	0.015	0.245	0.067	0.053	0.021	0.194	0.181	0.077	0.015	0.548	0.179	0.121	0.038	0.494

and ANN models offer intermediate performances, with the ANN sometimes approaching the DNN without, however, equaling it. Thus, the DNN model appears to be the most reliable and robust predictive tool for modeling the outputs studied.

The Taylor diagrams presented in Figure 10 compare the performance of four prediction models: RSM, ANN, DNN-IGWO, and SVM in terms of standard deviation and correlation coefficient. The DNN-IGWO model stands out as the best performer, as it faithfully reproduces the experimental data with a correlation coefficient close to 1 and a standard deviation almost identical to the reference. ANN follows closely, also showing high accuracy. The RSM models show intermediate performance, with moderate correlations and standard deviations somewhat far from the reference. Finally, SVM performs the worst, displaying a low correlation and an inadequate standard deviation. Overall, the neural network-based models (DNN-IGWO and ANN) significantly outperform conventional approaches, demonstrating their superiority for this prediction task.

6 GA multi-objective optimization results

The resolution of multi-objective optimization problems is now a central point in the analysis of most processes. Multi-objective optimization aims to maximize several components of a function vector. Unlike single-objective optimization, solving a multi-objective problem does not lead to a unique solution but instead leads to a set of solutions called the Pareto optimal solution set [99–101]. This section addresses the optimization of the physicomechanical properties of LFC using GAs based on empirical models obtained through ANN. GAs are highly efficient optimization methods for finding compromises and have become popular in the field of engineering optimization [102]. They replicate the principles of genetics and the Darwinian concept of natural selection (survival of the fittest). The first step is to arbitrarily select a population of initial solutions in the search space (the chromosomes) and then evaluate the performance of these solutions to create a new population of solutions by using evolutionary operators such as selection, crossover, and mutation [80,103,104]. This cycle (Figure 11) is repeated until a satisfactory solution is obtained.

The optimization process begins with data preprocessing, which involves collecting and preparing the input data required for training the ANN. Data normalization

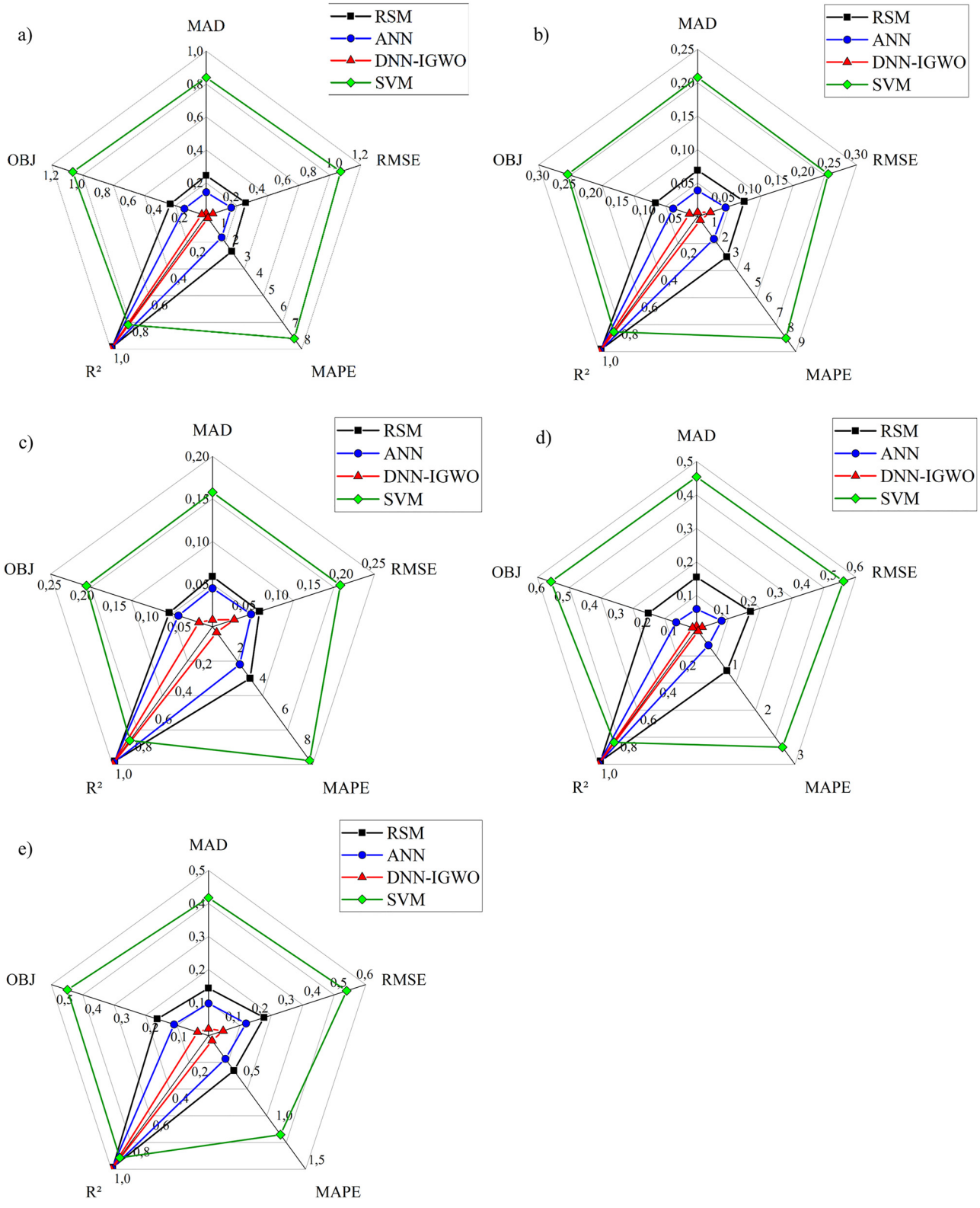

Figure 9: Spider plots of RSM, ANN, DNN-IGWO, and SVM for (a) CS, (b) FS, (c) STS, (d) WA, and (e) *P*.

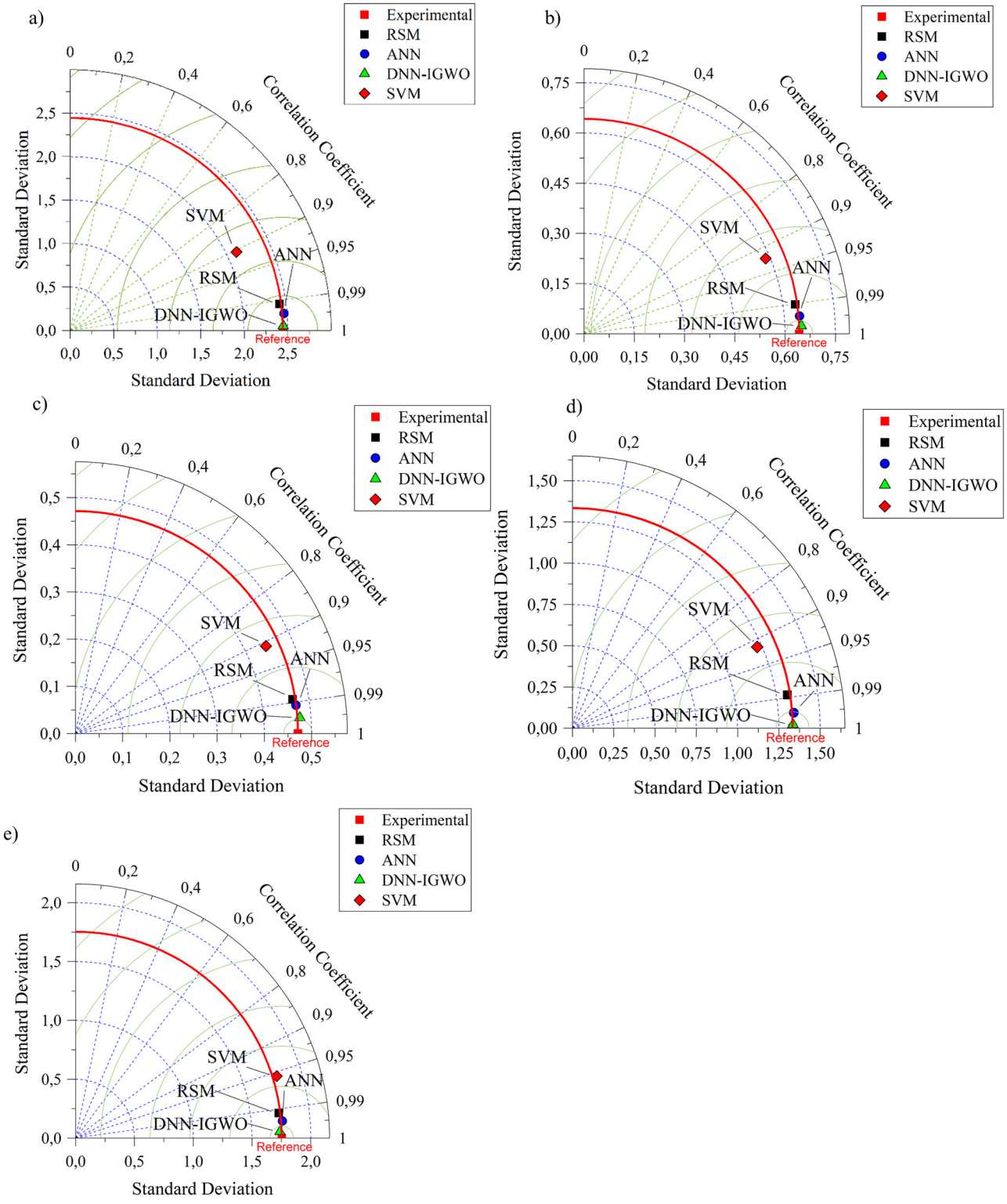

Figure 10: Taylor diagrams of RSM, ANN, DNN-IGWO, and SVM for (a) CS, (b) FS, (c) STS, (d) WA, and (e) *P*.

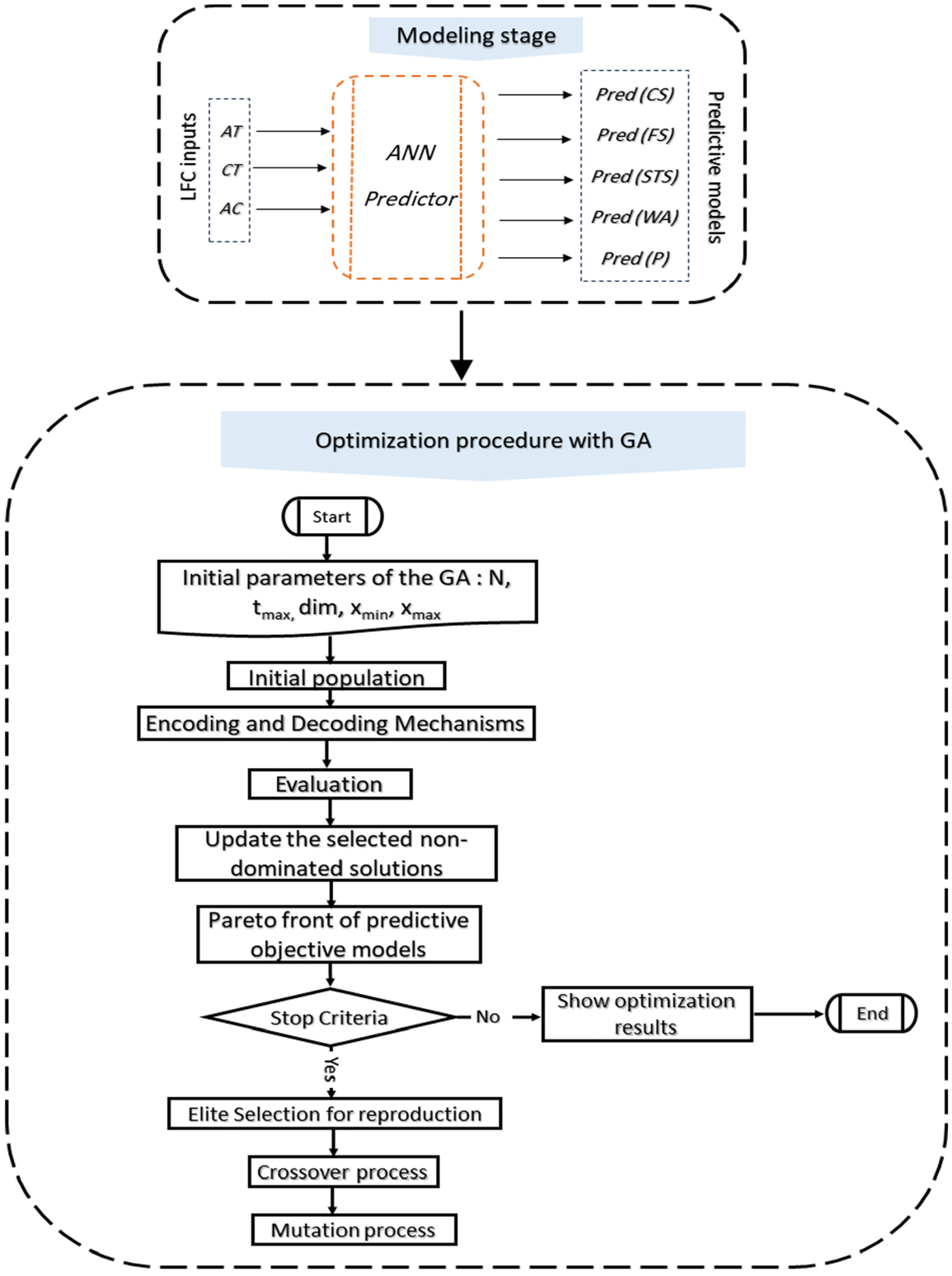

Figure 11: GAs flowchart for multi-objective optimization.

Table 15: Initial conditions for optimization by GA

Parameters	Objectives	Lower limit		Upper limit
Additive type	Gamme	OSA (1)	SSA (2)	MSA (3)
Curing time (days)	Gamme	7		28
Additive content (%)	Gamme	0		30
CS (MPa)	Max.	4.857		15.341
FS (MPa)	Max.	1.312		3.895
STS (MPa)	Max.	0.9377		2.861
WA (%)	Max.	15.7597		19.352
P (%)	Max.	35.219		40.426

is applied to ensure that all input variables are on a comparable scale. The dataset is then divided into training and testing sets to assess the performance of the ANN model.

Once the data are prepared, the next step is training the ANN model. The ANN is designed as a regression model to predict target output variables based on the input features. The training process involves adjusting the network weights to minimize prediction errors, typically using backpropagation and gradient descent algorithms. The trained ANN model is later incorporated into the fitness evaluation of the GA.

After training the ANN, the GA is initialized. The GA begins by generating an initial population of candidate

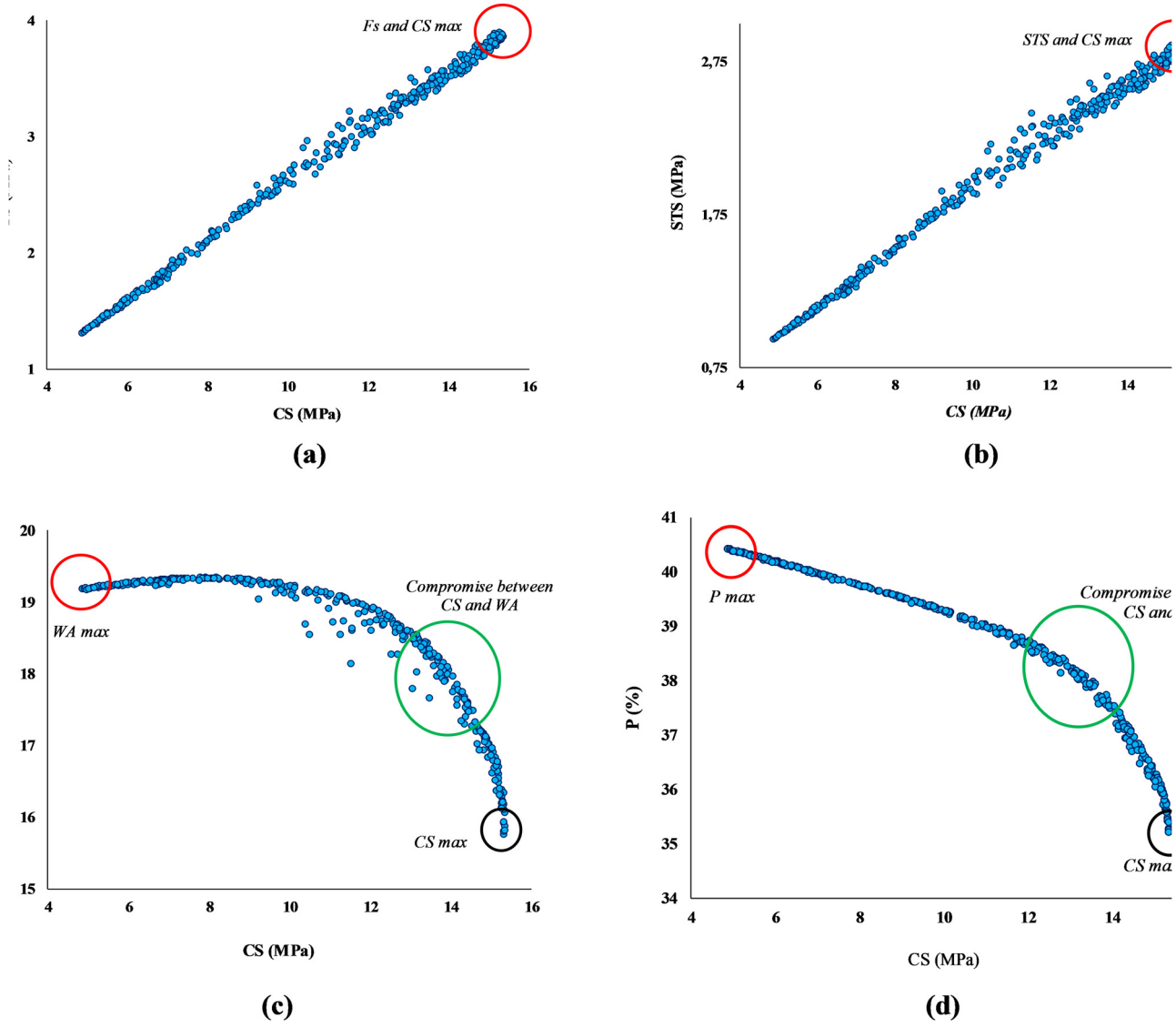

Figure 12: Pareto front graphs obtained by GA for CS: (a) FS, (b) STS, (c) WA, and (d) *P*.

solutions, each representing a set of potential model parameters or hyperparameters for optimization. A key element of the GA is the fitness function, which evaluates the performance of each candidate solution. In this case, the fitness function is based on the ANN model's accuracy in predicting the desired outputs. The GA is also configured with parameters such as the crossover rate, mutation rate, and the number of generations for evolution.

The next step is to evaluate the fitness of each individual in the population. Using the ANN model, the fitness of each candidate is assessed by comparing the predicted outputs to the actual target values. This process ensures that the GA selects candidate solutions that minimize errors while optimizing other objectives, such as improving CS and FS in the context of LFC.

Once the fitness evaluation is complete, the GA performs selection, where the top-performing candidates (parents) are chosen based on their fitness scores. Selection methods like roulette wheel or tournament selection are employed to increase the likelihood that individuals with better performance will pass their genes to the next generation [105,106].

Once the parents are selected, the crossover (recombination) process is applied, during which parent solutions are combined to generate offspring. Crossover enables the algorithm to explore new regions of the solution space by blending traits from two parent solutions, potentially yielding better-performing solutions in future generations.

To maintain diversity in the population and prevent premature convergence, a mutation step is introduced. In this stage, small random changes are made to some offspring to explore less-explored areas of the solution space. This randomness ensures that the algorithm avoids getting trapped in local optima and increases the likelihood of finding a global optimum [107,108].

The population is then updated with the newly generated offspring, replacing the previous generation. This iterative evolutionary process of selection, crossover, mutation, and population updating continues until a stopping criterion is met.

At the end of each iteration, a convergence check is performed to determine whether the stopping criteria – such as reaching a maximum number of generations or achieving a predefined threshold for improvement – have been satisfied. If the criteria are met, the optimization process concludes; otherwise, the algorithm returns to the fitness evaluation stage and proceeds with another iteration.

Once the algorithm converges, the optimized solution is obtained, representing the best-performing set of parameters for the ANN regression model. These parameters are then used to enhance the model's predictive accuracy while meeting the multi-objective optimization goals of the problem.

This section aims to identify all the optimal solutions that yield superior physicomechanical properties for LFC, including maximum CS, FS, tensile strength, WA, and *P*. The different optimization conditions are outlined in Table 15.

The Pareto fronts (2D) depicted in Figure 12(a)–(d) showcase various combinations of OBJs (CS *vs* FS, STS, WA, *P*). These fronts outline the spectrum of variation between two properties and are characterized by series of points. Each transition from one point to another represents an improvement in one OBJ at the expense of the other. The selection of a solution hinges on user preference. However, Pareto fronts offer significant utility by streamlining options and aiding decision-makers in pinpointing a desired operating point from the optimal Pareto point set [109,110].

Figure 12(a) and (b) depict the Pareto front for two sets of OBJs: CS *vs* FS, and CS *vs* STS. These graphs illustrate the relationship between these properties, showcasing the trade-offs that occur when attempting to optimize both simultaneously. When aiming to maximize both CS and FS or CS and STS, the Pareto front highlights regions were achieving higher values for both properties is feasible. Conversely, moving toward regions where both functions decrease signifies a compromise in the performance of the concrete mix. These insights are invaluable for decision-making, as they help in identifying the most favorable operating points and trade-offs based on project requirements and priorities [111,112].

Figure 12(c) and (d) depicts the Pareto front and reveal a fundamental trade-off between the two OBJs. In this scenario, maximizing one function inevitably leads to the minimization of the other. This relationship is evident between CS and WA, as well as CS and *P*. The Pareto front illustrates that achieving higher CS values corresponds to lower WA and *P* values. These findings underscore the inherent compromise involved in optimizing these properties simultaneously. Note that no single solution is superior; rather, the solutions represent compromises that need to be considered carefully based on specific project requirements and objectives [113–115].

7 Conclusion

This work explores the physicomechanical behavior of LFC with seashell ash as an additive, a waste product, in

concrete production to promote recycling of waste materials and reduce the reliance on cement that have high carbon footprint attending sustainable development goals (Nos 9, 11, 12, 13, and 15), this research helps in reducing gas emissions associated with cement production. RSM and ANN are employed to model and optimize mechanical strength, WA, and *P*. Multi-objective optimization using GA identifies optimal levels in LFC production. On the basis of experimental work, the following conclusions can be drawn:

- Curing time significantly influences the mechanical properties of LFC (CS, FS, and STS) by its contribution of 71.20, 77.89, and 78.06%, respectively. In contrast, additive content contributes 10.29, 7.12, and 5.02%, respectively, indicating its low impact on these properties.
- OSA, SSA, and MSA insignificantly (*P* value >0.05) affect CS, FS, and STS, respectively.
- Additive content exerts a greater influence on WA and *P* with 63.63 and 79.78%, respectively, compared with curing time of 18.34 and 10.42% and additive type of 1.86 and 1.40%, respectively.
- The highest CS, FS, and STS were achieved over a 28-day curing period and with an additive content ranging from 4 to 20%, in addition to substituting cement with three types of additives, namely, OSA, SSA, and MSA.
- For samples subjected to a 28-day curing period, additive content ranging from 18 to 30% and the presence of MSA showed lower WA of LFC than samples containing OSA and SSA.
- For samples subjected to a 28-day curing period, additive content ranging from 24 to 30%, with OSA and MSA, exhibited lower *P* of LFC compared with the sample containing SSA.
- The hybrid ANN (DNN-IGWO) demonstrated excellent accuracy and reliability in predicting experimental results. It was distinguished by a higher coefficient of determination (R^2) and significantly lower error values (MAD, RMSE, MAPE, and OBJ), thus outperforming RSM, ANN, and SVM models for all predicted LFC properties.
- The combined use of the hybrid ANN and the RSM method is recommended, as these approaches are complementary and contribute to enhancing the quality of the overall statistical analysis.
- The Pareto front analysis reveals a trade-off between maximizing the mechanical properties of LFC (CS, FS, and STS) and minimizing its physical properties (WA and *P*), emphasizing the conflicting nature of these objectives.

Acknowledgments: The authors extend their appreciation to Prince Sattam bin Abdulaziz University for funding this research work through the project number (PSAU/2024/01/31676).

Funding information: This study was supported by research fund from Prince Sattam bin Abdulaziz University, 2024.

Author contributions: Conceptualization: A.-M.M and B.-A.T.; methodology: Y.-C. and A.-L.; validation: B.-A.T.; formal analysis: Y.-I. A. and M.-O. B.; investigation: Y.-C., Y.-I. A., and A.-L.; resources: A.-M.M. and B.-A.T.; writing – original draft preparation: B.-A.T.; writing – review and editing: A.-M.M., Y.-I. A., and A.-L.; visualization: Y.-C, Y.-I. A., and A.-L.; project administration: B.-A.T.; and funding acquisition: A.-M.M. All authors have accepted responsibility for the entire content of this manuscript and approved its submission.

Conflict of interest: The authors state no conflict of interest.

Data availability statement: The datasets generated and/or analyzed during the current study are available from the corresponding author on reasonable request.

References

[1] Sunarno, Y., M. W. Tjaronge, R. Irmawaty, A. B. Muhiddin, M. A. Caronge, and M. Tumpu. Ultrasonic pulse velocity (UPV) and initial rate of water absorption (IRA) of foam concrete containing blended cement. *Materials Research Proceedings*, Vol. 31, 2023, pp. 571–580.

[2] Amran, M., R. Fediuk, N. Vatin, Y. Huei Lee, G. Murali, T. Ozbakkaloglu, et al. Fibre-reinforced foamed concretes: A review. *Materials (Basel)*, Vol. 13, 2020, id. 4323.

[3] Gencel, O., T. Bilir, Z. Bademler, and T. Ozbakkaloglu. A detailed review on foam concrete composites: Ingredients, properties, and microstructure. *Applied Sciences*, Vol. 12, 2022, id. 5752.

[4] Alharthai, M., M. A. O. Mydin, N. S. Alimrani, S. S. Majeed, and B. A. Tayeh. Evaluating deterioration of the properties of lightweight foamed concrete at elevated temperatures. *Journal of Building Engineering*, Vol. 84, 2024, id. 108515.

[5] Amran, Y. H. M., N. Farzadnia, and A. A. A. Ali. Properties and applications of foamed concrete; a review. *Construction and Building Materials*, Vol. 101, 2015, pp. 990–1005.

[6] Amran, M., Y. Huei Lee, N. Vatin, R. Fediuk, S. Poi-Ngian, Y. Yong Lee, et al. Design efficiency, characteristics, and utilization of reinforced foamed concrete: A review. *Crystals*, Vol. 10, 2020, id. 948.

[7] Hilal, A. A., N. H. Thom, and A. R. Dawson. Pore structure and permeation characteristics of foamed concrete. *Journal of Advanced Concrete Technology*, Vol. 12, 2014, pp. 535–544.

[8] Shankar, A. N., S. Chopade, R. Srinivas, N. K. Mishra, H. K. Eftikhaar, G. Sethi, et al. Physical and mechanical properties of foamed concrete, a literature review. *Materials Today: Proceedings*, Vol. 80, 2023, pp. 276–283.

[9] Raj, A., D. Sathyan, and K. M. Mini. Physical and functional characteristics of foam concrete: A review. *Construction and Building Materials*, Vol. 221, 2019, pp. 787–799.
[10] Mohammad, M. *Development of foamed concrete: enabling and supporting design*, University of Dundee, Dundee, United Kingdom, 2011.
[11] Priyatham, B., M. T. S. Lakshmayya, and D. Chaitanya. Review on performance and sustainability of foam concrete. *Materials Today: Proceedings*, University of Dundee, Dundee, United Kingdom, 2023.
[12] Hamad, A. J. Materials, production, properties and application of aerated lightweight concrete. *International Journal of Materials Science and Engineering*, Vol. 2, 2014, pp. 152–157.
[13] da Silva, A. L., E. R. Kohlman Rabbani, and M. Shakouri. Seashell powder as a sustainable alternative in cement-based materials: a systematic literature review. *Sustainability*, Vol. 17, 2025, id. 592.
[14] Poudel, S., U. Bhetuwal, P. Kharel, S. Khatiwada, D. KC, S. Dhital, et al. Waste glass as partial cement replacement in sustainable concrete: Mechanical and fresh properties review. *Buildings*, Vol. 15, 2025, id. 857.
[15] Tayeh, B. A., M. W. Hasaniyah, A. M. Zeyad, and M. O. Yusuf. Properties of concrete containing recycled seashells as cement partial replacement: A review. *Journal of Cleaner Production*, Vol. 237, 2019, id. 117723.
[16] Maglad, A. M., M. A. O. Mydin, S. D. Datta, and B. A. Tayeh. Assessing the mechanical, durability, thermal and microstructural properties of sea shell ash based lightweight foamed concrete. *Construction and Building Materials*, Vol. 402, 2023, id. 133018.
[17] Wijayasundara, M., P. Mendis, and R. H. Crawford. Methodology for the integrated assessment on the use of recycled concrete aggregate replacing natural aggregate in structural concrete. *Journal of Cleaner Production*, Vol. 166, 2017, pp. 321–334.
[18] Ahmed, M. M., K. A. M. El-Naggar, D. Tarek, A. Ragab, H. Sameh, A. M. Zeyad, et al. Fabrication of thermal insulation geopolymer bricks using ferrosilicon slag and alumina waste. *Case Studies in Construction Materials*, Vol. 15, 2021, id. e00737.
[19] Adewuyi, A. P., S. O. Franklin, and K. A. Ibrahim. Utilization of mollusc shells for concrete production for sustainable environment. *International Journal of Scientific Engineering and Research*, Vol. 6, 2015, pp. 201–208.
[20] Olutoge, F. A., O. M. Okeyinka, and O. S. Olaniyan. Assessment of the suitability of periwinkle shell ash (PSA) as partial replacement for ordinary Portland cement (OPC) in concrete. *International Journal of Research and Reviews in Applied Sciences*, Vol. 10, 2012, pp. 428–434.
[21] Hai-Yan, C., L. G. Li, Z.-M. Lai, A. K. H. Kwan, P.-M. Chen, and P. L. Ng. Effects of crushed oyster shell on strength and durability of marine concrete containing fly ash and blastfurnace slag. *Materials Science*, Vol. 25, 2019, pp. 97–107.
[22] Adeala, A. J. and J. O. Olaoye. Structural properties of snail shell ash concrete (SSAC). *Journal of Emerging Technologies and Innovative Research*, Vol. 6, 2019, pp. 24–31.
[23] Kellouche, Y., B. Boukhatem, M. Ghrici, R. Rebouh, and A. Zidol. Neural network model for predicting the carbonation depth of slag concrete. *Asian Journal of Civil Engineering*, Vol. 22, 2021, pp. 1401–1414.
[24] Sahraoui, M. and T. Bouziani. ANN modelling approach for predicting SCC properties-Research considering Algerian experience. Part II. Effects of aggregates types and contents. *Journal of Building Materials and Structures*, Vol. 8, 2021, pp. 63–71.
[25] Chetbani, Y., R. Zaitri, B. A. Tayeh, I. Y. Hakeem, F. Dif, and Y. Kellouche. Physicomechanical behavior of high-performance concrete reinforced with recycled steel fibers from twisted cables in the brittle state – experimentation and statistics. *Buildings*, Vol. 13, 2023, id. 2290.
[26] Hammoudi, A., K. Moussaceb, C. Belebchouche, and F. Dahmoune. Comparison of artificial neural network (ANN) and response surface methodology (RSM) prediction in compressive strength of recycled concrete aggregates. *Construction and Building Materials*, Vol. 209, 2019, pp. 425–436.
[27] Hameed, M. M., M. K. AlOmar, W. J. Baniya, and M. A. AlSaadi. Prediction of high-strength concrete: high-order response surface methodology modeling approach. *Engineering with Computers*, Vol. 38, 2022, pp. 1655–1668.
[28] Dean, A., D. Voss, D. Draguljić, A. Dean, D. Voss, and D. Draguljić. Response surface methodology. *Design and Analysis of Experiments*, Springer, Cham, 2017, pp. 565–614.
[29] Chelladurai, S. J. S., M. Kurugan, A. P. Ray, M. Upadhyaya, V. Narasimharaj, and S. Gnanasekaran. Optimization of process parameters using response surface methodology: A review. *Materials Today: Proceedings*, Vol. 37, 2021, pp. 1301–1304.
[30] Alaloul, W. S. and A. H. Qureshi. Data processing using artificial neural networks. *Dynamic data assimilation-beating the uncertainties*, IntechOpen, Dundee, United Kingdom, 2020.
[31] Micheli-Tzanakou, E. Artificial neural networks: an overview. *Network: Computation in Neural Systems*, Vol. 22, 2011, pp. 208–230.
[32] Zakaria, M., A. S. Mabrouka, and S. Sarhan. Artificial neural network: a brief overview. *Neural Networks*, Vol. 1, 2014, id. 2.
[33] Krenker, A., J. Bešter, and A. Kos. Introduction to the artificial neural networks. *Artificial neural networks: Methodological advances and biomedical applications*, InTech, Rijeka, Croatia, 2011, pp. 1–18.
[34] Biem, A. Neural networks: A review. *Data classification: Algorithms and applications*, CRC Press (Taylor & Francis Group), Boca Raton, Florida, USA, 2014, pp. 205–244.
[35] Apicella, A., F. Donnarumma, F. Isgrò, and R. Prevete. A survey on modern trainable activation functions. *Neural Networks*, Vol. 138, 2021, pp. 14–32.
[36] Rizalman, A. N. and C. C. Lee. Comparison of artificial neural network (ANN) and response surface methodology (RSM) in predicting the compressive strength of POFA concrete. *Applications of Modelling and Simulation*, Vol. 4, 2020, pp. 210–216.
[37] Yaro, N. S. A., M. H. Sutanto, N. Z. Habib, M. Napiah, A. Usman, and A. Muhammad. Comparison of Response Surface Methodology and Artificial Neural Network approach in predicting the performance and properties of palm oil clinker fine modified asphalt mixtures. *Construction and Building Materials*, Vol. 324, 2022, id. 126618.
[38] Ray, S., M. Haque, T. Ahmed, and T. T. Nahin. Comparison of artificial neural network (ANN) and response surface methodology (RSM) in predicting the compressive and splitting tensile strength of concrete prepared with glass waste and tin (Sn) can fiber. *Journal of King Saud University-Engineering Sciences*, Vol. 35, 2023, pp. 185–199.
[39] British Standard Institution. *Cement composition, specifications and conformity criteria for common cements (BS EN 17-1:2019)*, BSI, 2019. https://www.en-standard.eu/bs-en-197-1-2011-cement-

composition-specifications-and-conformity-criteria-for-common-cements/(accessed September 15, 2024).
[40] A. Commitee, C09. *ASTM C33-03, Standard specifications for concrete agregates*, ASTM Int, West Conshohocken, Pennsylvania, USA, 2003.
[41] BS 3148:1980. *Methods of test for water for making concrete (including notes on the suitability of the water) (withdrawn)*, British Standards Institution - Publication Index | NBS, n.d. https://www.thenbs.com/PublicationIndex/documents/details?Pub=BSI&DocId=11281 (accessed September 15, 2024).
[42] BSI, BS EN 12390-3. *Testing hardened concrete. Part 3: Compressive strength of test specimens*, British Standards Institution (BSI), London, United Kingdom, 2009.
[43] B.S. En, 12390-5. *Testing hardened concrete–Part 5: flexural strength of test specimens*, Br. Stand. Institution-BSI CEN Eur. Comm. Stand, London, United Kingdom, 2009.
[44] E.N. CSN, 12390-6. *Testing hardened concrete-Part 6: Tensile splitting strength of test specimens*, Czech Office for Standards, Metrology and Testing (ÚNMZ), Czech Repub, 2009.
[45] C1403. *Standard test method for rate of water absorption of masonry mortars*, n.d. https://www.astm.org/c1403-15.html (accessed September 15, 2024).
[46] Kim, J., D.-G. Kim, and K. H. Ryu. Enhancing response surface methodology through coefficient clipping based on prior knowledge. *Processes*, Vol. 11, 2023, id. 3392.
[47] Chiappini, F. A., S. M. Azcarate, C. M. Teglia, and H. C. Goicoechea. Fundamentals of design of experiments and optimization: Data modeling in response surface methodology. In *Introduction to quality by design in pharmaceutical manufacturing and analytical development*, Springer, Cham, Switzerland, 2023, pp. 67–89.
[48] Taavitsainen, V.-M. T. Experimental optimization and response surfaces. *Chemometrics in practical applications*, IntechOpen, Dundee, United Kingdom, 2012, pp. 91–138.
[49] Hong, W. C., B. S. Mohammed, I. Abdulkadir, and M. S. Liew. Modeling and optimizing the effect of palm oil fuel ash on the properties of engineered cementitious composite. *Buildings*, Vol. 13, 2023, id. 628.
[50] Zhang, Y., Q. Zhang, A. H. AlAteah, A. Essam, and S. A. Mostafa. Predictive modeling for mechanical characteristics of ultra high-performance concrete blended with eggshell powder and nano silica utilizing traditional technique and machine learning algorithm. *Case Studies in Construction Materials*, Vol. 21, 2024, id. e04025.
[51] Gupta, A. K. Predictive modelling of turning operations using response surface methodology, artificial neural networks and support vector regression. *International Journal of Production Research*, Vol. 48, 2010, pp. 763–778.
[52] Chetbani, Y., M. Boumaaza, R. Zaitri, A. Belaadi, A. Ben Mahammed, A. Laouissi, et al. Study of the effect of hemp fibers and brick waste powder on the mechanical characteristics of mortar: experimental and statistical analysis. *Journal of Natural Fibers*, Vol. 22, 2025, id. 2438900.
[53] Brahimi, M., R. Benderradji, E. Raouache, Y. Chetbani, A. Laouissi, and A. J. Chamkha. A numerical study and statistical approach of the impact of nanofluids on mixed convection in a ventilated cavity. *The International Journal of Advanced Manufacturing Technology*, Vol. 134, 2024, pp. 5281–5300.
[54] Bensmail, M., R. Zaitri, M. Hani, Y. Chetbani, D. Benamara, and A. Laouissi. Analyzing the effects of recycled aggregates on the workability and mechanical characteristics of concrete through mixture design and optimization techniques. *World Journal of Engineering*, Vol. 74, 2025, pp. 255–260.
[55] Ben Salah, H. and M. Hani. An investigation of the effect of high temperature on the strength compression and ultrasonic pulse velocity of self-compacting concrete. *The Journal of Engineering and Exact Sciences*, Vol. 10, 2024, id. 16818.
[56] Alem, D. D. An overview of data analysis and interpretations in research. *International Journal of Academic Research in Education and Review*, Vol. 8, 2020, pp. 1–27.
[57] Bertinetto, C., J. Engel, and J. Jansen. ANOVA simultaneous component analysis: A tutorial review. *Analytica Chimica Acta: X*, Vol. 6, 2020, id. 100061.
[58] Mezaouri, S., S. M. Aissa Mamoune, H. Siad, M. Lachemi, M. Boumaaza, A. Belaadi, et al. Prediction of cementitious composite characteristics based on waste glass powder and aggregates: Experimental and statistical analysis. *Measurement*, Vol. 224, 2025, id. 117609.
[59] Saiah, W., A. Rabahi, M. Boumaaza, M. Hani, A. Belaadi, Y. Chetbani, et al. Antioxidant, anti-inflammatory, and anti-diabetic assessment of (2Z)-2 (arylimino)-2Hchromene-3-carboxamides: An in vitro-in silico study by applying ANN-GA, MCDM, and RSM optimization techniques. *Results in Chemistry*, Vol. 6, 2025, id. 102249.
[60] Myers, J. L., A. D. Well, and R. F. Lorch Jr. *Research design and statistical analysis*, Routledge, New York, USA, 2013.
[61] Nanda, A., B. B. Mohapatra, A. P. K. Mahapatra, A. P. K. Mahapatra, and A. P. K. Mahapatra. Multiple comparison test by Tukey's honestly significant difference (HSD): Do the confident level control type I error. *International Journal of Statistics and Applied Mathematics*, Vol. 6, 2021, pp. 59–65.
[62] Lee, D. K. Alternatives to *P* value: confidence interval and effect size. *Korean Journal of Anesthesiology*, Vol. 69, 2016, id. 555.
[63] Bouyaya, L., A. Belaadi, M. Boumaaza, A. Lekrine, B. X. Chai, Y. Chetbani, et al. Chemical processing effect on the tensile strength of waste palm fiber-reinforced HDPE biocomposite: Optimizing using response surface methodology. *Journal of Natural Fibers*, Vol. 21, 2024, id. 2421810.
[64] Kellouche, Y., B. A. Tayeh, Y. Chetbani, A. M. Zeyad, and S. A. Mostafa. Comparative study of different machine learning approaches for predicting the compressive strength of palm fuel ash concrete. *Journal of Building Engineering*, Vol. 88, 2024, id. 109187.
[65] Nwadiugwu, M. C. Neural networks, artificial intelligence and the computational brain. *arXiv preprint arXiv:2101.08635*, 2020.
[66] Arshavsky, Y. I. Neurons versus networks: The interplay between individual neurons and neural networks in cognitive functions. *The Neuroscientist*, Vol. 23, 2017, pp. 341–355.
[67] Yang, G. R. and X.-J. Wang. Artificial neural networks for neuroscientists: a primer. *Neuron*, Vol. 107, 2020, pp. 1048–1070.
[68] Montesinos López, O. A., A. Montesinos López, and J. Crossa. Fundamentals of artificial neural networks and deep learning. In *Multivariate statistical machine learning methods for genomic prediction*, Springer, Cham, Switzerland, 2022, pp. 379–425.
[69] Taherdoost, H. Deep learning and neural networks: Decision-making implications. *Symmetry (Basel)*, Vol. 15, 2023, id. 1723.
[70] Qamar, R. and B. A. Zardari. Artificial neural networks: An overview. *Mesopotamian Journal of Computer Science*, Vol. 2023, 2023, pp. 124–133.
[71] Laouissi, A., M. M. Blaoui, H. Abderazek, M. Nouioua, and A. Bouchoucha. Heat treatment process study and ANN-GA

based multi-response optimization of C45 steel mechanical properties. *Metals And Materials International*, Vol. 28, 2022, pp. 3087–3105.
[72] Thakur, A. and A. Konde. Fundamentals of neural networks. *International Journal for Research in Applied Science and Engineering Technology*, Vol. 9, 2021, pp. 407–426.
[73] Worden, K., G. Tsialiamanis, E. J. Cross, and T. J. Rogers. Artificial neural networks. In *Machine learning in modeling and simulation: Methods and applications*, Springer, Cham, Switzerland, 2023, pp. 85–119.
[74] Lyu, Z., Y. Yu, B. Samali, M. Rashidi, M. Mohammadi, T. N. Nguyen, et al. Back-propagation neural network optimized by *K*-fold cross-validation for prediction of torsional strength of reinforced concrete beam. *Materials (Basel)*, Vol. 15, 2022, id. 1477.
[75] Nti, I. K., O. Nyarko-Boateng, and J. Aning. Performance of machine learning algorithms with different *K* values in *K*-fold cross-validation. *International Journal of Information Technology and Computer Science*, Vol. 6, 2021, pp. 61–71.
[76] Raschka, S. Model evaluation, model selection, and algorithm selection in machine learning. *arXiv preprint arXiv:1811.12808*, 2018.
[77] Jung, Y. Multiple predicting *K*-fold cross-validation for model selection. *Journal of Nonparametric Statistics*, Vol. 30, 2018, pp. 197–215.
[78] Pandian, S. *K-fold cross validation technique and its essentials*. analyticsvidhya.com, 2022.
[79] Hakmi, T., A. Hamdi, A. Laouissi, H. Abderazek, S. Chihaoui, and M. A. Yallese. Mathematical modeling using ANN based on k-fold cross validation approach and MOAHA multi-objective optimization algorithm during turning of polyoxymethylene POM-C. *Jordan Journal of Mechanical & Industrial Engineering*, Vol. 18, 2024, pp. 179–190.
[80] Laouissi, A., M. A. Yallese, A. Belbah, S. Belhadi, and A. Haddad. Investigation, modeling, and optimization of cutting parameters in turning of gray cast iron using coated and uncoated silicon nitride ceramic tools. Based on ANN, RSM, and GA optimization. *The International Journal of Advanced Manufacturing Technology*, Vol. 101, 2019, pp. 523–548.
[81] Marcot, B. G. and A. M. Hanea. What is an optimal value of k in k-fold cross-validation in discrete Bayesian network analysis? *Computational Statistics*, Vol. 36, 2021, pp. 2009–2031.
[82] Pal, K. and B. V. Patel. Data classification with k-fold cross validation and holdout accuracy estimation methods with 5 different machine learning techniques. In *2020 Fourth International Conference on Computing Methodologies and Communication (ICCMC)*, IEEE, 2020, pp. 83–87.
[83] Dastres, R. and M. Soori. Artificial neural network systems. *International Journal of Imaging and Robotics*, Vol. 21, 2021, pp. 13–25.
[84] Abdolrasol, M. G. M., S. M. S. Hussain, T. S. Ustun, M. R. Sarker, M. A. Hannan, R. Mohamed, et al. Artificial neural networks based optimization techniques: A review. *Electronics*, Vol. 10, 2021, id. 2689.
[85] Panda, S. and G. Panda. Fast and improved backpropagation learning of multi-layer artificial neural network using adaptive activation function. *Expert Systems*, Vol. 37, 2020, id. e12555.
[86] Ionin, A. S., L. N. Karelina, N. S. Shuravin, M. S. Sidel'nikov, F. A. Razorenov, S. V. Egorov, et al. Experimental study of the transfer function of a superconducting Gauss neuron prototype. *JETP Letters*, Vol. 118, 2023, pp. 766–772.
[87] Dubey, S. R., S. K. Singh, and B. B. Chaudhuri. Activation functions in deep learning: A comprehensive survey and benchmark. *Neurocomputing*, Vol. 19, 2022, pp. 1–19.
[88] Reffas, O., H. Boumediri, Y. Karmi, M. S. Kahaleras, I. Bousba, and L. Aissa. Statistical analysis and predictive modeling of cutting parameters in EN-GJL-250 cast iron turning: application of machine learning and MOALO optimization. *The International Journal of Advanced Manufacturing Technology*, Vol. 137, 2025, pp. 1–19.
[89] Karmi, Y., H. Boumediri, O. Reffas, Y. Chetbani, S. Ataya, R. Khan, et al. Integration of hybrid machine learning and multi-objective optimization for enhanced turning parameters of EN-GJL-250 cast iron. *Crystals*, Vol. 15, 2025, id. 264.
[90] Touati, S., H. Boumediri, Y. Karmi, M. Chitour, K. Boumediri, A. Zemmouri, et al. Performance analysis of steel W18CR4V grinding using RSM, DNN-GA, KNN, LM, DT, SVM models, and optimization via desirability function and MOGWO. *Heliyon*, Vol. 11, 2025, id. e42640.
[91] Eade, E. Gauss-Newton/Levenberg-Marquardt optimization. *Tech. Rep.*, 2013, pp. 1–14.
[92] de Jesús Rubio, J. Stability analysis of the modified Levenberg–Marquardt algorithm for the artificial neural network training. *IEEE Transactions on Neural Networks and Learning Systems*, Vol. 32, 2020, pp. 3510–3524.
[93] Awad, M. and R. Khanna. Support vector machines for classification. In *Efficient learning machines: Theories, concepts, and applications for engineers and system designers*, Springer, New York, USA, 2015, pp. 39–66.
[94] Syam, N. and R. Kaul. Support vector machines in marketing and sales. In *Machine learning and artificial intelligence in marketing and sales*, Emerald Publishing Limited, Bingley, United Kingdom, 2021, pp. 85–137.
[95] Otchere, D. A., T. O. A. Ganat, R. Gholami, and S. Ridha. Application of supervised machine learning paradigms in the prediction of petroleum reservoir properties: Comparative analysis of ANN and SVM models. *Journal of Petroleum Science & Engineering*, Vol. 200, 2021, id. 108182.
[96] Cortes, C. and V. Vapnik. Support-vector networks. *Machine Learning*, Vol. 20, 1995, pp. 273–297.
[97] Raouache, E., A. Laouissi, F. Khalfallah, and Y. Chetbani. Development and optimization of a prediction system model for mechanical properties in rotary friction-welded polyamide joints using the SVM approach and GA optimization. *International Journal of Advanced Manufacturing Technology*, Vol. 132, 2024, pp. 1005–1017.
[98] Çaydaş, U. and S. Ekici. Support vector machines models for surface roughness prediction in CNC turning of AISI 304 austenitic stainless steel. *Journal of Intelligent Manufacturing*, Vol. 23, 2012, pp. 639–650.
[99] Deb, K., K. Sindhya, and J. Hakanen. Multi-objective optimization. In *Decision sciences*, CRC Press, Boca Raton, Florida, USA, 2016, pp. 161–200.
[100] Taha, K. Methods that optimize multi-objective problems: A survey and experimental evaluation. *IEEE Access*, Vol. 8, 2020, pp. 80855–80878.
[101] Azzouz, R., S. Bechikh, and L. Ben Said. Dynamic multi-objective optimization using evolutionary algorithms: a survey. *Recent advances in evolutionary multi-objective optimization*, Springer, Cham, Switzerland, 2017, pp. 31–70.
[102] Wang, Z. and A. Sobey. A comparative review between Genetic Algorithm use in composite optimisation and the state-of-the-art in evolutionary computation. *Composite Structures*, Vol. 233, 2020, id. 111739.

[103] Gupta, S. K. An overview of genetic algorithms: a structural analysis. *International Journal of Innovative Science and Research Technology*, Vol. 15, 2021, id. 58.
[104] Türkoğlu, B. and H. Eroğlu. Genetic Algorithm for Route Optimization. In *Applied genetic algorithm and its variants: Case studies and new developments*, Springer, Singapore, 2023, pp. 51–79.
[105] Tamaki, H., H. Kita, and S. Kobayashi. Multi-objective optimization by genetic algorithms: A review. In *Proceedings of IEEE International Conference on Evolutionary Computation*, IEEE, 1996, pp. 517–522.
[106] Konak, A., D. W. Coit, and A. E. Smith. Multi-objective optimization using genetic algorithms: A tutorial. *Reliability Engineering & System Safety*, Vol. 91, 2006, pp. 992–1007.
[107] Xu, M. *Advancing genetic programming for learning scheduling heuristics*, Victoria University of Wellington, Wellington, New Zealand, 2024.
[108] Zhang, W., G. Xiao, M. Gen, H. Geng, X. Wang, M. Deng, et al. Enhancing multi-objective evolutionary algorithms with machine learning for scheduling problems: recent advances and survey. *Frontiers in Industrial Engineering*, Vol. 2, 2024, id. 1337174.
[109] Rahim, A. A. A., S. N. Musa, S. Ramesh, and M. K. Lim. A systematic review on material selection methods. *Proceedings of the Institution of Mechanical Engineers, Part L: Journal of Materials: Design and Applications*, Vol. 234, 2020, pp. 1032–1059.
[110] Li, Y., J. Baik, M. M. Rahman, I. Anagnostopoulos, R. Li, and T. Shu. Pareto optimization of CNN models via hardware-aware neural architecture search for drainage crossing classification on resource-limited devices. In *Proceedings of the SC'23 Workshops of the International Conference on High Performance Computing, Network, Storage, and Analysis*, 2023, pp. 1767–1775.
[111] Mattson, C. A. and A. Messac. Pareto frontier based concept selection under uncertainty, with visualization. *Optimization and Engineering*, Vol. 6, 2005, pp. 85–115.
[112] Rebello, C. M., M. A. F. Martins, D. D. Santana, A. E. Rodrigues, J. M. Loureiro, A. M. Ribeiro, et al. From a pareto front to pareto regions: A novel standpoint for multiobjective optimization. *Mathematics*, Vol. 9, 2021, id. 3152.
[113] Ngatchou, P., A. Zarei, and A. El-Sharkawi. Pareto multi objective optimization. In *Proceedings of the 13th International Conference on, Intelligent Systems Application to Power Systems*, IEEE, 2005, pp. 84–91.
[114] Guédas, B. and P. Dépincé. A compromise definition in multiobjective multidisciplinary design optimization. In *8th World Congress on Structural and Multidisciplinary Optimization*, 2009.
[115] Ciftcioglu, Ö. and M. S. Bittermann. Adaptive formation of Pareto front in evolutionary multi-objective optimization. *Evolutionary Computation*, Vol. 17, 2009, pp. 417–444.